Title

Profiling presynaptic scaffolds using split-GFP reconstitution reveals cell-type-specific spatial configurations in the fly brain

Authors

Hongyang Wu[1], Yoh Maekawa[2], Sayaka Eno[1], Shu Kondo[3], Nobuhiro Yamagata[1,4], Hiromu Tanimoto[1,2]*

Affiliations

[1] Graduate School of Life Sciences, Tohoku University, Sendai, Japan.

[2] Department of Biology, Faculty of Science, Tohoku University, Sendai, Japan.

[3] Department of Biological Science and Technology, Tokyo University of Science, Tokyo, Japan.

[4] Department of Life Science, Graduate School of Engineering Science, Akita, Akita University.

* Correspondence: Dr. Hiromu Tanimoto (hiromut@m.tohoku.ac.jp)

Abstract

Characterization of intracellular synapse heterogeneity aides to understand the intricate computational logic of neuronal circuits. Despite recent advances in connectomics, the spatial patterns of synapses and their inter-individual variability remain largely unknown. Using directed split-GFP reconstitution, we achieved visualization of endogenous Bruchpilot (Brp), a presynaptic active zone (AZ) scaffold protein, in a cell-type-specific manner. By developing a high-throughput quantification pipeline, we profiled AZ structures in identified neurons of the mushroom body circuit, where intracellular synaptic patterns are crucial due to compartmentalized connectivity. Quantitative characterization of the pattern of Brp clusters across multiple individuals revealed cell-type-dependent synapse heterogeneity and stereotypy. Furthermore, we discovered previously unidentified sub-compartmental synapse configuration and its transient structural plasticity triggered by associative learning. These profiles thus uncovered multi-layered spatial configurations of AZs, from stereotyped overall AZ distribution patterns, to local arrangements of neighboring synapses.

Keywords:

Intracellular synaptic configuration; synapse profiling; active zones; Bruchpilot; mushroom body circuit; split-GFP; synapse heterogeneity; synapse stereotypy; structural plasticity; associative learning

Introduction

The brain is a complex network of neurons, and understanding their wiring strategies provides crucial insights into their roles in neuronal computation. Release sites in the presynaptic terminal of *Drosophila* neurons are decorated with electron-dense projections composed of active-zone (AZ) scaffolds that are essential for efficient synaptic transmission (Akbergenova et al., 2018; Fouquet et al., 2009; Kittel et al., 2006; Matkovic et al., 2013; Newman et al., 2022; Paul et al., 2015; Wagh et al., 2006). These dense projections serve as a synapse marker enabling the whole-brain connectomes,

comprehensive mapping of synaptic connections at the electron microscopic level (Dorkenwald et al., 2024; Scheffer et al., 2020; Schlegel et al., 2024; Takemura et al., 2024; Zheng et al., 2018). While connectome-based approaches catalyzed the exploration of cell type distinctions, circuit motifs, and neurotransmitters, their application to comparisons across different conditions is still challenging due to the limited throughput of data acquisition and dense reconstruction. Since the synaptic structure and connectivity reflect substantial variability of development and experiences (Fernández et al., 2008; Gilestro et al., 2009; Kremer et al., 2010; Sachse et al., 2007; Schlegel et al., 2024; Turrel et al., 2022; Zhang et al., 2018), cross-individual comparisons are necessary. Fluorescence labeling offers high throughputs and contents, especially when comparing synaptic organizations across cell-types (Mosca and Luo, 2014) or brain regions (Gao et al., 2019). Nevertheless, characterizing endogenous synaptic proteins in specific cells using fluorescence-labeling remains challenging in the central nervous system (CNS). This has driven growing interest in designing cell-type-specific fluorescence-tagging strategies for endogenous synaptic protein (Chen et al., 2014).

The circuit of *Drosophila* mushroom bodies (MBs) plays a central role in olfactory associative learning (Davis, 2023). The major intrinsic MB neuron, known as Kenyon cells (KCs) respond to odor stimulation and synapse onto the spatially segregated dendrites of MB output neurons (MBONs) that divide the MB into compartments. Distinct types of dopaminergic neurons (DANs) synapse onto specific compartments and thereby modulate KC-MBON synapses in the corresponding compartments (Aso et al., 2014). Presynaptic calcium levels of these DANs undergo sub-compartmental GABAergic modulation and inform memory specificity, postulating the distinct synapse structures at individual release sites (Yamagata et al., 2021) . Two types of giant interneurons, the anterior paired lateral neuron (APL) and the dorsal paired medial (DPM) neuron extensively ramify across the MB lobes and provide recurrent modulations to KC synapses (Haynes et al., 2015; Keene et al., 2006, 2004; Lin et al., 2014; Liu and Davis, 2009; Pitman et al., 2011; Waddell et al., 2000; Yu et al., 2005). Considering their comprehensive projections throughout the MB lobes, the modulation of local circuits requires intracellular synaptic tuning. These studies

together underscore the importance to spatially distinguish individual synapses within a cell. However, the high AZ density in the MB lobes precluded conventional approaches of fluorescent microscopy from profiling synaptic structures of specific neurons (Scheffer et al., 2020).

Here, we present a spatial analysis of individual AZs within the MB circuit at the single-cell resolution, achieved by cell-type-specific visualization of the endogenous active zone protein Bruchpilot (Brp) using the CRISPR/Cas9-mediated split-GFP tagging system. *Drosophila* ELKS/CAST/ERC family member Brp plays a central role in molecular assemblies at AZs by accumulating calcium channels and synaptic vesicles (Fouquet et al., 2009; Hallermann et al., 2010; Kittel et al., 2006; Matkovic et al., 2013; Wagh et al., 2006). Therefore, Brp enrichment serve as a structural proxy suited for estimating synapse function, such as release probability at single AZs (Akbergenova et al., 2018; Newman et al., 2022). We developed a high-throughput quantification pipeline to systematically profile Brp clusters of individual AZs in different MB-innervating neurons. Characterizing the distinct parameters and localization of Brp clusters revealed AZ distribution stereotypy across individuals and significant synaptic heterogeneity within single neurons. These cell-type-specific synapse profiles suggest that AZs are spatially organized at multiple scales, ranging from interindividual stereotypy to neighboring synapses in the same cells.

Results

Establishing an experimental system for cell-type-specific profiling of active zone structures

As the molecular assembly of synapses is reported to be sensitive to the dosage of Brp, we visualized endogenous Brp instead of transgenic expression of tagged Brp (Huang et al., 2020). To label endogenous Brp specifically in designated cell types, we employed the split-GFP tagging system (Kamiyama et al., 2016; Kondo et al., 2020) . Using CRISPR/Cas9, we inserted the GFP_{11} fragment (the eleventh β-strand of the super-folder GFP) just prior to the stop codon of *brp* gene. The GFP_{1-10} fragment is expressed in cells of interest by the GAL4/UAS system. The self-assembly of the split-GFP fragments is

106 therefore directed only in GAL4-expressing cells and visualizes endogenous Brp through
107 reconstituted GFP fluorescence (Figure 1A).
108 As a proof of principle, we first validated the localization and plasticity of split-GFP
109 tagged Brp (Figure 1B). To verify tagged Brp localization in an individual neuron, we
110 directed GFP reconstitution and expressed a plasma membrane marker in the serotonergic
111 DPM neuron using *VT64246-GAL4* (Figure 1C). Confocal microscopy revealed
112 Brp::reconstituted GFP (Brp::rGFP) signals only to the MB lobes, aligning with DPM
113 terminals (Waddell et al., 2000). These signals were distributed as discrete clusters within
114 plasma membrane varicosities resembling presynaptic boutons (Figure 1C), suggesting that
115 Brp::rGFP clusters labeled individual AZs in the DPM neuron. AZ localization of
116 Brp::rGFP was further validated by co-localization with anti-Brp immunostaining in the
117 calyx and the voltage-gated calcium channel subunit Cacophony (Cac) in the PAM
118 dopaminergic neurons (Figure 1D-E) (Kawasaki et al., 2004; Kittel et al., 2006). We found
119 that GFP_{11} tagging did not affect *brp* mRNA levels, but slightly decreased protein
120 expression without altering overall expression pattern in the brain (Figure 1 – figure
121 supplement 1-2). Brp::rGFP successfully visualized previously reported light-induced AZ
122 plasticity in the photoreceptors (Sugie et al., 2015). Constant light exposure reduced the
123 numbers of Brp::rGFP clusters in the R8 terminals in the medulla, compared to constant
124 darkness (DD) (Figure 1F). This was further substantiated by increased Brp::rGFP cluster
125 intensities upon knocking-down *rab3* expression (Figure 1 – figure supplement 3),
126 recapitulating Rab3-dependent regulation of Brp allocation in the presynaptic terminals of
127 the motor neurons (Graf et al., 2009).
128 To systematically profile Brp::rGFP clusters, we developed an image processing
129 pipeline (Figure 1A). In brief, image deconvolution was applied to reduce out-of-focus light
130 and enhance signal sharpness (Figure 1 – figure supplement 4). Individual Brp::rGFP
131 clusters were then segmented using the 3D suite plugin in Fiji (Ollion et al., 2013),
132 generating the 3D region-of-interests (3D ROIs) that encircle each cluster. Brp::rGFP signal
133 intensity, volume and location of individual clusters were measured using the 3D ROIs. To
134 optimize the segmentation, we systematically varied the parameters and calculated the F-

135 score to measure detection accuracy against manually defined ground truth (see Materials
136 and Methods). The F-score is near 1.0 in segmenting Brp::rGFP clusters within DPM and
137 APL neurons and achieved > 0.90 in KCs with certain combinations of segmentation
138 parameters (Figure 1 – figure supplement 5).
139 To confirm that Brp clusters represent AZs, we quantified the numbers of
140 Brp::rGFP clusters in DPM and APL neurons specifically and compared them to the
141 connectome data. We found that cluster counts closely matched the number of AZs
142 annotated by the hemibrain connectome (Figure 1C) (Scheffer et al., 2020). This result
143 validated our method that accurately isolated Brp::rGFP clusters corresponding to single
144 AZs.
145
146 **AZ profiles within KCs are compartmentally heterogeneous**
147 Brp accumulation at individual AZs is known to be heterogeneous even within a single
148 motor neuron (Akbergenova et al., 2018; Ehmann et al., 2014; Gratz et al., 2019; Paul et al.,
149 2015). To study such AZ heterogeneity in CNS neurons, we quantified the signal intensity
150 of individual Brp::rGFP clusters in MB lobes. Using KC subtype-specific drivers to direct
151 split-GFP reconstitution in γ KC (*MB009B-GAL4*), α'/β' KCs (*MB370B-GAL4*) and α/β
152 KCs (*MB008B-GAL4*). we found that within-cluster Brp::rGFP intensities are highly
153 diverse in all KC subtypes (Figure 2A).
154 To visualize spatial patterns of Brp::rGFP intensity in each KC subtype, we
155 reconstructed 3D distribution of Brp::rGFP clusters and color-coded them by signal
156 intensities (Figure 2B). We found that clusters showed noticeable intensity differences
157 between compartments in all subtypes. Even adjacent compartments such as γ1 and γ2, β'2
158 and β'1, α2 and α3, showed drastic differences (Figure 2B). Importantly, these
159 compartmental patterns were stable across individuals (Figure 2C) (Wu et al., 2025). This
160 result suggests that AZs in different compartments have distinct structures. Since individual
161 KCs of each subtype synapse onto all compartments (Scheffer et al., 2020; Schlegel et al.,
162 2023; Takemura et al., 2024; Zheng et al., 2018), this Brp compartmental heterogeneity is
163 likely formed intracellularly.

164

165 **Intracellular heterogeneity of Brp concentration at individual AZs and cell-type**
166 **dependent diversity**

167 Super-resolution microscopy has shown that the Brp molecular density at individual AZs is
168 dynamically adjusted in motor neurons (Ghelani et al., 2023; Mrestani et al., 2021). We
169 hypothesized that the amount of Brp does not necessarily correlate with AZ cluster size. To
170 verify this, we calculated the Brp concentration by quantifying both the volume (number of
171 voxels within a 3D ROI) and the Brp::rGFP intensity of each cluster. We found that
172 clusters with similar sizes can exhibit vastly different signal intensities in the DPM neuron,
173 suggesting the heterogeneity of Brp concentration at individual AZs (Figure 3A).
174 Correlation analysis between the Brp::rGFP intensity and cluster volume revealed a
175 substantial variability among cell types (Figure 3B-E). There were even significant
176 differences among KC subtypes. These results suggest cell-type dependent variability of the
177 Brp concentration of individual clusters.

178

179 **Stereotypy of intracellular distribution of AZs**

180 To study the spatial distribution of Brp clusters within single neurons, we focused on
181 DANs. *MB504B-GAL4* labels four types of single PPL1 DANs projecting to distinct
182 compartments (Vogt et al., 2014). Using this driver, we analyzed Brp::rGFP distribution in
183 each compartment and found it uneven in terminals of both PPL1-α2α'2 and α3 (Figure 4A-
184 B). To better characterize cluster distribution, we calculated the "AZ density" defined as
185 the number of Brp::rGFP clusters surrounding a particular cluster within a specified radius
186 (see Figure 1A and Materials and Methods for detail). By color-coding Brp::rGFP clusters
187 according to their AZ density, we found that AZs in PPL1-α3 were more localized to the
188 core of the α3 compartment. This pattern was consistent across individuals (Figure 4C-D),
189 suggesting a stereotyped AZ distribution within PPL1-α3 neurons.

190 We extended the analysis to two other single pairs of neurons innervating the MBs,
191 the DPM and APL neurons. Visualizing AZ density revealed a stereotyped and
192 compartment specific distribution in the DPM neuron (Figure 5A). Specifically, the AZ

density was constantly high in the α'/β' lobes across all individuals, supporting the known functional importance of DPM branches in the α'/β' lobes (Keene et al., 2006). In contrast, this compartmental pattern was less pronounced in the APL neuron. Notably, the ratio of AZ density between α3 and α'3 is strikingly different among individuals (Figure 5B). Taken together, these data suggest that the individual variability in AZ distribution depends on the cell type.

Regulation of spatial configuration of AZs

Characteristics of Brp clusters and AZ distribution in KCs revealed spatial organization at the level of compartments. Recent studies further showed intra-compartmental variability of synaptic plasticity upon associative learning, prompting us to analyze sub-compartmental organization of AZs (Bilz et al., 2020; Davidson et al., 2023). We thus examined potential local patterns among AZs in proximity by calculating the correlation between nearest neighbor clusters in terms of their Brp::rGFP intensities (Figure 6A-B). This analysis revealed strong correlations in KCs and APL but not in DPM (Figure 6C).

We further analyzed the sub-compartmental AZ patterns by examining the spatial distribution of Brp::rGFP intensity. To reduce the high frequency variability of Brp::rGFP intensities (Figure 2B), we calculated the "local intensity" for each cluster by applying mean filtering (the average Brp::rGFP intensity of all surrounding clusters within a specified radius *r*, see Materials and Methods for detail). By visualizing the local intensity in γ KCs, we identified AZ "hot spots", sub-compartment-sized small groups of AZs with high local intensities, on top of the compartmental differences (Figure 6D). Since Brp molecules are clustered more in AZ-dense boutons of a single motor neuron (Paul et al., 2015), we hypothesized that these hot spots correspond to regions with higher AZ densities. Indeed, we found that hot spots appear in high AZ densities regions in γ KCs (Figure 6D). Consistently, correlation between the local intensity and the AZ density was high in all KC subtypes. In contrast, for DPM and APL neurons, the local intensity of Brp::rGFP was not associated with AZ density (Figure 6E-H). Taken together, these results suggest previously unidentified sub-compartmental synaptic configuration organized across individual KCs.

222

223 **Associative learning re-organizes sub-compartmental synaptic configuration**

224 Sub-compartmental synaptic configuration may undergo experience-dependent changes,
225 such as through associative learning (Turrel et al., 2022; Zhang et al., 2018). To examine
226 such structural plasticity in local AZ configurations (Figure 6D, F-H), we visualized
227 Brp::rGFP specifically in KCs using *R13F02-GAL4* (Figure 7A). This induction did not
228 alter MB morphology and short-term memory compared to wild-type (Figure 7 – figure
229 supplement 1-2). We presented flies with odor (4-methylcyclohexanol) with a concomitant
230 (paired) or shifted (unpaired) electric shock (Fig. 7B). Since both paired and unpaired
231 groups were exposed to the same odor and electric shock, the difference between these
232 groups purely represents the effect of association. As single odor conditioning induced
233 memory decaying gradually over one day (Figure 7B), we measured the correlation
234 between the AZ density and local intensity of individual Brp::rGFP clusters (Figure 6F-H)
235 at different time points after conditioning (from 3 min to 1 day). Strikingly, we found that
236 associative learning induced a transient modification to the KC synaptic configurations in a
237 compartment-specific manner (Figure 7C). This learning-induced structural plasticity was
238 specific at 90 min after conditioning and disappeared within one day (Figure 7D),
239 consistent with previous studies reporting short-lived AZ remodeling in the MBs by
240 conditioning (Turrel et al., 2022; Zhang et al., 2018). These results showcase the advantage
241 of split-GFP system in reporting the dynamics of local synapse subsets with high
242 throughputs and contents. Altogether, we suggest that associative learning induces transient
243 memory traces of local structural plasticity in AZ configuration.

244

245 **Discussion**

246 By leveraging the CRISPR/Cas9 genome editing of the *brp* locus and split-GFP technique,
247 we systematically profiled presynaptic structures of MB neurons in a cell-type-specific
248 manner. This approach enabled high-throughput analysis of multiple brain samples and
249 detailed characterizations, revealing previously inaccessible structural features of AZs in
250 CNS neurons. Cell-type specific labeling of other endogenous synaptic proteins, such as

251 vesicle-associated proteins, may provide complementary insights to AZ profiling and allow
252 molecular reconstruction of synapses.

253 Single-cell level analysis of AZ profiles revealed cell-type-specific stereotypy in
254 spatial regulation (Figure 4-6). We found that AZ density in the DPM neurons is
255 consistently high in the α'/β' lobes across individuals (Figure 5). This AZ stereotypy of
256 DPM explains the functional significance of the branches in the α'/β' lobes. Overexpression
257 of a Down syndrome cell adhesion molecule (DScam) variant in the DPM neurons was
258 shown to disrupt their innervation except in the α'/β' lobe, while memory formation
259 remained unaffected (Keene et al., 2006). Similarly, our analysis identified the intracellular
260 stereotypy in AZ distribution of the PPL1-α3 DAN within the α3 compartment (Figure 4).
261 This sub-compartmental organization of the single DAN and layered projections of α/β
262 KCs may underlie the differential dopaminergic modulation of KC subtypes in associative
263 learning (Perisse et al., 2013). While such stereotypy is less pronounced in APL, we found
264 strong correlations between Brp::rGFP intensities of neighboring AZs in contrast to DPM
265 (Figure 6D). This suggests that AZs in APL neurons are organized more locally, allowing
266 them to modulate microcircuits composed of KCs, DANs and MBONs (Amin et al., 2020).
267 Collectively, the spatial scale of AZ organizations depends on cell types, reflecting the
268 function of individual MB neurons.

269 We observed that Brp::rGFP intensity correlates strongly with the AZ size in KC
270 subtypes, in contrast to DPM and APL neurons (Figure 3). Previous studies using
271 localization microscopy showed that the molecular density of synaptic proteins at AZs can
272 be dynamically adjusted in motor neurons, potentially modulating the synaptic vesicle
273 release (Ghelani et al., 2023; Mrestani et al., 2021; Sachidanandan et al., 2023). The
274 variable Brp concentrations (i.e. the ratio of the Brp::rGFP intensity to the AZ size) in DPM
275 and APL neurons may represent AZs with distinct Brp densities and therefore different
276 functional modes (Figure 3) (Mrestani et al., 2021). Notably, a recent study successfully
277 predicted the neurotransmitter type of neurons using the ultrastructure of dense projections
278 as one of the parameters (Eckstein et al., 2024), suggesting neurotransmitter-specific AZ
279 structures. Interestingly, both the DPM and APL neurons are reported to release multiple

neurotransmitters (Davie et al., 2018; Haynes et al., 2015; Lee et al., 2011; Liu and Davis, 2009; Wu et al., 2013; Zeng et al., 2023). Distinct Brp concentrations at AZs might thus support particular release modes or neurotransmitter types.

In KCs, the spatial analysis of local AZ configuration revealed strong correlations between Brp::rGFP intensities at neighboring AZs as well as AZ "hot spots", regions with high Brp localization and AZ densities (Figure 6). These results suggest previously unidentified, highly localized sub-compartmental AZ structures, which are likely organized across individual KCs. Presynaptic terminals of a single KC are found to be highly heterogeneous in terms of their plasticity upon dopamine modulation and associative learning (Bilz et al., 2020; Davidson et al., 2023). A recent study found the sub-compartmentally heterogeneous activities of dopamine terminals explain memory specificity (Yamagata et al., 2021). Such locally distinct dopamine input may be a source of the AZ hot spot formation in KC terminals. This model is consistent with the localization of two opposing dopamine receptors Dop1R1 and Dop2R to AZs (Hiramatsu et al., 2024). Furthermore, we showed that the local configuration undergoes structural plasticity upon associative learning that involves presynaptic dopaminergic modulation (Aso et al., 2012, 2010; Aso and Rubin, 2016; Burke et al., 2012; Liu et al., 2012; Yamagata et al., 2015) (Figure 7). Since cAMP signaling plays a crucial role in the AZ structural plasticity especially during associative memory formation (Baltruschat et al., 2021; Sachidanandan et al., 2023; Wu et al., 2025), it may underlie learning-induced plasticity in sub-compartmental AZ configuration (Turrel et al., 2022; Zhang et al., 2018).

Materials and Methods

Animals

Flies were maintained on standard cornmeal food at 25 °C under a 12:12 h light-dark cycle for all experiments. All flies used for experiments are 3-7 days old adult males. Flies were transferred to fresh food vials after hatching and flipped every two days before experiments. The GAL4-UAS system was used to express transgenes, and balancers were removed for animals used in all experiments. Fly strains and resources used in this study are as follow: *MB008B-GAL4* (BDSC 68291) (Aso et al., 2014), *MB009B-GAL4* (BDSC 68292) (Aso et al., 2014); *MB370B-GAL4* (BDSC 68319) (Aso et al., 2014), *MB504B-GAL4* (BDSC 68329) (Aso et al., 2014) , *VT64246-GAL4* (VDRC 204311) (Tirian and Dickson, 2017), *GH146-GAL4* (BDSC 30026) (Stocker et al., 1997), *R58E02-GAL4* (BDSC 41347) (Pfeiffer et al., 2008), *R13F02-GAL4* (BDSC 48571) (Pfeiffer et al., 2008), *R86E01-GAL4* (BDSC 45914) (Jenett et al., 2012), *Amon-GAL4* (BDSC 30554) (Rhea et al., 2010) , *Rh6-GAL4* (BDSC 7464, by Dr. Claude Desplan), *UAS-CD4::tdTomato* (BDSC 35841, by Dr. Yhu Nung Jan & Chun Han), *UAS-Rab3-RNAi* (BDSC 34655) (Perkins et al., 2015), *brp::GFP*$_{11}$ (This study and (Wu et al., 2025)), *UAS-GFP*$_{1-10}$ (Kondo et al., 2020).

Generation of *brp::GFP*$_{11}$

CRISPR/Cas9-mediated homologous recombination was used to insert GFP_{11} right before the stop codon of *brp*. The donor vector contained a left homology arm of 747 bp, the GFP11 sequence (Kondo et al., 2020), a floxed 3xP3-RFP marker and a right homology arm of 741 bp. A guide RNA sequence (TCGCAAAGCCACAGATACAC) targeting the *brp* locus was cloned into pBFv-U6.2 (Kondo and Ueda, 2013) to generate a gRNA expression vector. The donor and gRNA vectors were co-injected into fertilized eggs carrying the nos-Cas9 transgene (Kondo and Ueda, 2013). Successful transformants were identified by eye-specific RFP fluorescence. Flies were then crossed to a CyO-Cre balancer to remove the RFP marker. Primers used to clone homology arms are as followed (lowercase letters indicate homologous recombination regions with the doner vector): left

330 arm forward: gcttgatatcgaattcAAGGACATCGAGGAAAAGGAGAAGAAG; left arm
331 reverse: agttgggggcgtaggGAAAAAGCTCTTCAAGAAGCCAGCTGGTCC; right arm
332 forward: tagtataggaacttcTCGCAAAGCCACAGATACACACATCTTGG; right arm
333 reverse: cgggctgcaggaattcATCGTCGATAATTGTAAGTGCATGCTG
334

335 **qRT-PCR experiment**

336 Procedures are as previously described (Saito et al., 2025). For each sample, RNA extract
337 from ~20 heads was purified using TRIzol LS Reagent (Invitrogen) and Direct-zol RNA
338 Microprep kit (ZYMO RESEARCH), following the provided protocol. The concentration
339 of extracted RNA samples was then measured using the NanoDrop Spectrophotometer
340 (Thermo Fisher Scientific) and adjusted to a similar level using diluted water. Reverse
341 transcription was performed using ReverTra Ace qPCR RT Master Mix (TOYOBO, FSQ-
342 301). qRT-PCR was performed using iTaq Universal SYBR Green Supermix (BIO-RAD)
343 and CFX96 Touch Real-Time PCR Detection System (BIO-RAD). No template controls
344 were also prepared and measured alongside. Three primer pairs for *brp* were designed and
345 used in the experiment but only one pair that had Ct<30 for all samples was used. Primers
346 for *brp*, forward: AGCTCAAGGACCACATGGACATC; reverse:
347 GCGCCATATCCACCTGGTTGTC (Signma-Aldrich). Primers for *Ubiquitin-5E*, forward:
348 TCTTCACTTGGTCCTGCGTC; reverse: ATGGCTCGACCTCCAAAGTG (eurofins
349 Genomics). Primers for *αTubulin84B*, forward: GATCGTGTCCTCGATTACCGC;
350 reverse: GGGAAGTGAATACGTGGGTAGG (eurofins Genomics).
351

352 **Light exposure experiment**

353 Procedures are as previously described (Sugie et al., 2015). In brief, animals hatched within
354 one day were transferred to constant darkness (DD, 0 LUX) or constant light (LL, 2000-
355 4000 LUX by LED panels) environment at 25 °C and kept for 2-3 days. Animals were then
356 dissected and Brp::rGFP cluster number in individual R8 photoreceptor terminals in the
357 medulla was quantified.
358

359 **Associative conditioning**

360 For experiments in Figure 7C-D, adult flies at 3-7 days after eclosion were kept in a 25 °C
361 incubator before and after conditioning. Approximately 50 flies were put in a training tube
362 that is set inside the climate box for 2 minutes before the conditioning. Temperature in the
363 climate box was set at 24 °C and the relative humidity was set to 70%. For the paired
364 group, 2% 4-methycyclohexanol (4-MCH, Sigma-Aldrich, diluted in paraffin oil, Sigma-
365 Aldrich) was presented in a cup with the diameter of 5 mm, together with 12 pulses of
366 electric shocks at 90 V for 1 minute inside the training tube. The unpaired group received
367 the same 1-minute electric shock first, followed by 1-minute rest, and then the same 1-
368 minute 4-MCH presentation. Flies were dissected at 3 min, 20 min, 90 min, 270 min and 1
369 day after conditioning. Experiments were performed multiple times on different days for a
370 single group.

371 For measuring the memory decay curve of single odor conditioning, 2% 4-MCH
372 and pure paraffin oil were used for the training. One odor was presented with electric
373 shocks for 1 minute, followed by 1 minute rest, then another odor was presented without
374 electric shocks. For each reciprocal, preference was tested between 2% 4-MCH and
375 paraffin oil. For the differential odor conditioning and short-term memory performance test,
376 10% 4-MCH and 10% 3-OCT were used for the conditioning, following the same training
377 protocol. Short-term memory performance was tested immediately after the conditioning.
378 Performance index was calculated as $\#(CS-) - \#(CS+)/\#(CS-) + \#(CS+)$.

379

380 **Sample preparation**

381 Animals used in experiments involving comparisons between control and experimental
382 groups were dissected on the same day. Data were collected from multiple batches of
383 experiments performed on different days. Flies were anesthetized by ice and placed on ice
384 before dissection. The dissection was performed in cold PBS to collect the brain without
385 the ventral nerve cord. The brains were subsequently fixed by 2% paraformaldehyde for 1 h
386 and then washed 3×20 min by 0.1% PBT (0.1% Triton X-100 in PBS) in a PCR tube,
387 typically 5-6 brains in one tube. Samples were mounted on microscope slides using

388 mounting medium SeeDB2S (Ke et al., 2016). For nc82 immunostaining, fixed brains were
389 washed 3×20 min with 0.1% PBT and incubated in 3% normal goat serum (NGS; Sigma-
390 Aldrich; G9023)-0.1% PBT blocking solution for 1 hour at room temperature. The nc82
391 antibody (DSHB) solution was diluted 1:20 in the blocking solution. Samples were
392 incubated in antibody solutions at 4°C for 48 hours for both primary and secondary
393 antibodies.
394
395 **Confocal imaging**
396 The image acquisition was performed using an Olympus FV1200 confocal microscope
397 platform equipped with both PMT and GaAsP high sensitivity detectors and a 60×/1.42 NA
398 oil immersion objective (PLAPON60XO, Olympus). The Kalman filter was turned on to 2×
399 averaging while scanning. For imaging Brp::rGFP clusters in MB-projecting neurons,
400 scanning speed was set at 2~4 μs/pixel with a voxel size of lateral 0.079 × 0.079 × axial
401 0.370 μm. For experimental point spread function (PSF) imaging, SeeDB2S immersed
402 beads were scanned in a setting that is 60×/1.42 NA oil immersion objective; 473 nm laser
403 power: 2.0%; 559 nm laser power: 1.5%; voxel size: 0.079 μm × 0.079 μm × 0.370 μm;
404 scanning speed: 4 μs/pixel, to produce multiple bead images.
405
406 **PSF acquisition and image deconvolution**
407 Sub-resolution fluorescent beads (Tetraspeck Microspheres 0.1 μm, Thermo Fisher
408 Scientific, T7279) were imaged to generate the PSF. The bead solution was diluted with
409 distilled water and sonicated several times to eliminate aggregation. PSF images acquired
410 were processed using Amira software (Thermo Fisher Scientific) with the Extract Point
411 Spread Function module. The PSFs extracted from each image were averaged to create a
412 single PSF for later image deconvolution (Resizing voxel size: 0.079 μm × 0.079 μm ×
413 0.370 μm; 32 pixels × 32 pixels × 21 slices of image size). Image deconvolution was
414 performed by using the Richardson-Lucy iterative non-blind algorithm in a Fiji plugin
415 DeconvolutionLab2 (Sage et al., 2017), or by CLIJ2 GPU-based Richardson-Lucy

416 deconvolution (Haase et al., 2020). Images were deconvolved 20 times iteratively to
417 improve image quality.
418
419 **Brp clusters segmentation and data analysis**
420 For Brp::rGFP cluster detection, the image stack size was adjusted to double the XY plate
421 pixel number using Fiji to increase the detection precision. The images were subsequently
422 processed using the "3D maxima finder" and the "3D spot segmentation" function of the
423 "3D suite" package in Fiji. 3D maxima were identified for each cluster and used as the
424 starting point for pixel clustering (Ollion et al., 2013). An intensity threshold (threshold)
425 was first set to reduce noise. Pixels having values below the threshold would become NaN
426 (not a number). The "noise tolerance" was then set in the 3D maxima finder to adjust its
427 sensitivity. To be noticed, threshold is only applied to images processed by the 3D maxima
428 finder to generates the "peak" image stack. 3D spot segmentation function uses both the
429 "peak" image and the deconvolved Brp::rGFP image to generate "3D ROIs". 3D ROIs were
430 then applied on the raw images to quantify the volume (total voxel number in ROI) and
431 Brp::rGFP intensity (total pixel value in ROI) of individual clusters using the "3D ROI
432 manager". For processing most images, both threshold and noise tolerance were set to
433 200~400, where the segmentation was optimal based on the F-score benchmarking. "Local
434 thresholding method" in 3D spot segmentation was set to "Gaussian fit", and "SD value"
435 was set to 2.
436 The above procedures may include a tiling and stitching step for images and data
437 because of the limited computer power. Typically, an image was tiled into 25 sub-stacks
438 with overlapped margins. After being processed separately, the data acquired from all tiled
439 sub-stacks was stitched back with a deletion of overlapping data points to generate the
440 complete detection result. Nearest neighbors were identified for each particle and spatial
441 distances in between (NND) were calculated using Python. For each sample, mean NND
442 was calculated separately. For a particular Brp::rGFP cluster, the number of surrounding
443 clusters within r ($r = 3 \times$ mean NND) spherically including itself is referred as the "AZ
444 density". The "local intensity" of a particular Brp::rGFP cluster is the average of Brp::rGFP

445 intensity of all clusters surrounding within r (r = 3 × mean NND) including itself. The plot
446 function of Python was used to plot the color-coded 3D reconstructions. A sample code for
447 analyzing NND, AZ density and local intensity is provided with a demonstration data sheet
448 (Supplementary file 1 and analysis code).
449

450 **Detection optimization**

451 The 3D detection parameters were optimized by matching the 3D maxima detection results
452 to the ground truths. Ground truths were defined by annotating AZs manually, according to
453 the size, position and signal pattern of Brp clusters in the images. The F-score was used to
454 assess detection precision. F-score is the harmonic mean of a system's precision and recall
455 value, calculated by the following formula: 2 × [(Precision × Recall) / (Precision + Recall)].
456 The precision is the number of true positives divided by the total number of identified
457 positives, including incorrect identification. The recall is the number of true positives
458 divided by the total number of true data points defined as the ground truth. F-scores shown
459 in Figure S5 were automatically calculated using a customized Fiji Marco that aligned 3D
460 maxima with ground truth. Different combinations of noise threshold and noise tolerance
461 were tested for the test images cropped from raw images.
462

463 **Statistical analysis**

464 Statistical analysis was performed using GraphPad Prism version 8, 9 and 10 or Python.
465 For statistical comparisons, Kruskal-Wallis test with original False Discovery Rate method
466 of Benjamini and Hochberg correction was applied unless otherwise specified. The desired
467 false discovery rate was set to 0.05. Pearson's correlation coefficient (R) was calculated
468 using Python.
469

470 **References**

471
472

473 Akbergenova Y, Cunningham KL, Zhang YV, Weiss S, Littleton JT. 2018.
474 Characterization of developmental and molecular factors underlying release
475 heterogeneity at Drosophila synapses. *Elife* **7**:e38268. doi:10.7554/elife.38268

476 Amin H, Apostolopoulou AA, Suárez-Grimalt R, Vrontou E, Lin AC. 2020. Localized
477 inhibition in the Drosophila mushroom body. *Elife* **9**:e56954. doi:10.7554/elife.56954

478 Aso Y, Hattori D, Yu Y, Johnston RM, Iyer NA, Ngo T-T, Dionne H, Abbott L, Axel R,
479 Tanimoto H, Rubin GM. 2014. The neuronal architecture of the mushroom body
480 provides a logic for associative learning. *Elife* **3**:e04577. doi:10.7554/elife.04577

481 Aso Y, Herb A, Ogueta M, Siwanowicz I, Templier T, Friedrich AB, Ito K, Scholz H,
482 Tanimoto H. 2012. Three Dopamine Pathways Induce Aversive Odor Memories with
483 Different Stability. *PLoS Genet* **8**:e1002768. doi:10.1371/journal.pgen.1002768

484 Aso Y, Rubin GM. 2016. Dopaminergic neurons write and update memories with cell-type-
485 specific rules. *Elife* **5**:e16135. doi:10.7554/elife.16135

486 Aso Y, Siwanowicz I, Bräcker L, Ito K, Kitamoto T, Tanimoto H. 2010. Specific
487 Dopaminergic Neurons for the Formation of Labile Aversive Memory. *Curr Biol*
488 **20**:1445–1451. doi:10.1016/j.cub.2010.06.048

489 Baltruschat L, Prisco L, Ranft P, Lauritzen JS, Fiala A, Bock DD, Tavosanis G. 2021.
490 Circuit reorganization in the Drosophila mushroom body calyx accompanies memory
491 consolidation. *Cell Reports* **34**:108871. doi:10.1016/j.celrep.2021.108871

492 Bilz F, Geurten BRH, Hancock CE, Widmann A, Fiala A. 2020. Visualization of a
493 Distributed Synaptic Memory Code in the Drosophila Brain. *Neuron* **106**:963-976.e4.
494 doi:10.1016/j.neuron.2020.03.010

495 Burke CJ, Huetteroth W, Owald D, Perisse E, Krashes MJ, Das G, Gohl D, Silies M, Certel
496 S, Waddell S. 2012. Layered reward signalling through octopamine and dopamine in
497 Drosophila. *Nature* **492**:433–437. doi:10.1038/nature11614

498 Chen Y, Akin O, Nern A, Tsui CYK, Pecot MY, Zipursky SL. 2014. Cell-type-Specific
499 Labeling of Synapses In Vivo through Synaptic Tagging with Recombination. *Neuron*
500 **81**:280–293. doi:10.1016/j.neuron.2013.12.021

501 Davidson AM, Kaushik S, Hige T. 2023. Dopamine-Dependent Plasticity Is
502 Heterogeneously Expressed by Presynaptic Calcium Activity across Individual Boutons
503 of the Drosophila Mushroom Body. *eNeuro* **10**:ENEURO.0275-23.2023.
504 doi:10.1523/eneuro.0275-23.2023

Davie K, Janssens J, Koldere D, Waegeneer MD, Pech U, Kreft Ł, Aibar S, Makhzami S, Christiaens V, González-Blas CB, Poovathingal S, Hulselmans G, Spanier KI, Moerman T, Vanspauwen B, Geurs S, Voet T, Lammertyn J, Thienpont B, Liu S, Konstantinides N, Fiers M, Verstreken P, Aerts S. 2018. A Single-Cell Transcriptome Atlas of the Aging Drosophila Brain. *Cell* **174**:982-998.e20. doi:10.1016/j.cell.2018.05.057

Davis RL. 2023. Learning and memory using Drosophila melanogaster : a focus on advances made in the fifth decade of research. *GENETICS*. doi:10.1093/genetics/iyad085

Dorkenwald S, Matsliah A, Sterling AR, Schlegel P, Yu Szi-chieh, McKellar CE, Lin A, Costa M, Eichler K, Yin Y, Silversmith W, Schneider-Mizell C, Jordan CS, Brittain D, Halageri A, Kuehner K, Ogedengbe O, Morey R, Gager J, Kruk K, Perlman E, Yang R, Deutsch D, Bland D, Sorek M, Lu R, Macrina T, Lee K, Bae JA, Mu S, Nehoran B, Mitchell E, Popovych S, Wu J, Jia Z, Castro MA, Kemnitz N, Ih D, Bates AS, Eckstein N, Funke J, Collman F, Bock DD, Jefferis GSXE, Seung HS, Murthy M, Dorkenwald S, Matsliah A, Sterling AR, Schlegel P, Yu Szi-chieh, McKellar CE, Lin A, Costa M, Eichler K, Yin Y, Silversmith W, Schneider-Mizell C, Jordan CS, Brittain D, Halageri A, Kuehner K, Ogedengbe O, Morey R, Gager J, Kruk K, Perlman E, Deutsch D, Bland D, Sorek M, Lu R, Macrina T, Lee K, Bae JA, Mu S, Nehoran B, Mitchell E, Popovych S, Wu J, Jia Z, Castro MA, Kemnitz N, Ih D, Bates AS, Eckstein N, Funke J, Collman F, Bock DD, Jefferis GSXE, Seung HS, Murthy M, Lenizo Z, Burke AT, Willie KP, Serafetinidis N, Hadjerol N, Willie R, Silverman B, Ocho JA, Bañez J, Candilada RA, Kristiansen A, Panes N, Yadav A, Tancontian R, Serona S, Dolorosa JI, Vinson KJ, Garner D, Salem R, Dagohoy A, Skelton J, Lopez M, Capdevila LS, Badalamente G, Stocks T, Pandey A, Akiatan DJ, Hebditch J, David C, Sapkal D, Monungolh SM, Sane V, Pielago ML, Albero M, Laude J, Santos M dos, Vohra Z, Wang K, Gogo AM, Kind E, Mandahay AJ, Martinez C, Asis JD, Nair C, Patel D, Manaytay M, Tamimi IFM, Lim CA, Ampo PL, Pantujan MD, Javier A, Bautista D, Rana R, Seguido J, Parmar B, Saguimpa JC, Moore M, Pleijzier MW, Larson M, Hsu J, Joshi I, Kakadiya D, Braun A, Pilapil C, Gkantia M, Parmar K, Vanderbeck Q, Salgarella I, Dunne C, Munnelly E, Kang CH, Lörsch L, Lee J, Kmecova L, Sancer G, Baker C, Joroff J, Calle S, Patel Y, Sato O, Fang S, Salocot J, Salman F, Molina-Obando S, Brooks P, Bui M, Lichtenberger M, Tamboboy E, Molloy K, Santana-Cruz AE, Hernandez A, Yu Seongbong, Diwan A, Patel M, Aiken TR, Morejohn S, Koskela S, Yang T, Lehmann D, Chojetzki J, Sisodiya S, Koolman S, Shiu PK, Cho S, Bast A, Reicher B, Blanquart M, Houghton L, Choi H, Ioannidou M, Collie M, Eckhardt J, Gorko B, Guo L, Zheng Z, Poh A, Lin M, Taisz I, Murfin W, Díez ÁS, Reinhard N, Gibb P, Patel N, Kumar S, Yun M, Wang M, Jones D, Encarnacion-Rivera L, Oswald A, Jadia A, Erginkaya M, Drummond N, Walter L, Tastekin I, Zhong X, Mabuchi Y, Santiago FJF, Verma U, Byrne N, Kunze E, Crahan T, Margossian R, Kim H, Georgiev I, Szorenyi F, Adachi A, Bargeron B, Stürner T, Demarest D, Gür B, Becker AN, Turnbull R, Morren A, Sandoval A, Moreno-Sanchez A, Pacheco DA, Samara E, Croke H, Thomson A, Laughland C, Dutta SB, Antón PGA de, Huang B, Pujols P, Haber I, González-Segarra

547 A, Choe DT, Lukyanova V, Mancini N, Liu Z, Okubo T, Flynn MA, Vitelli G, Laturney
548 M, Li F, Cao S, Manyari-Diaz C, Yim H, Le AD, Maier K, Yu Seungyun, Nam Y, Bąba
549 D, Abusaif A, Francis A, Gayk J, Huntress SS, Barajas R, Kim M, Cui X, Sterne GR, Li
550 A, Park K, Dempsey G, Mathew A, Kim Jinseong, Kim T, Wu G, Dhawan S, Brotas M,
551 Zhang C, Bailey S, Toro AD, Yang R, Gerhard S, Champion A, Anderson DJ, Behnia
552 R, Bidaye SS, Borst A, Chiappe E, Colodner KJ, Dacks A, Dickson B, Garcia D,
553 Hampel S, Hartenstein V, Hassan B, Helfrich-Forster C, Huetteroth W, Kim Jinseop,
554 Kim SS, Kim Y-J, Kwon JY, Lee W-C, Linneweber GA, Maimon G, Mann R, Noselli
555 S, Pankratz M, Prieto-Godino L, Read J, Reiser M, Reyn K von, Ribeiro C, Scott K,
556 Seeds AM, Selcho M, Silies M, Simpson J, Waddell S, Wernet MF, Wilson RI, Wolf
557 FW, Yao Z, Yapici N, Zandawala M. 2024. Neuronal wiring diagram of an adult brain.
558 *Nature* **634**:124–138. doi:10.1038/s41586-024-07558-y

559 Eckstein N, Bates AS, Champion A, Du M, Yin Y, Schlegel P, Lu AK-Y, Rymer T, Finley-
560 May S, Paterson T, Parekh R, Dorkenwald S, Matsliah A, Yu S-C, McKellar C, Sterling
561 A, Eichler K, Costa M, Seung S, Murthy M, Hartenstein V, Jefferis GSXE, Funke J.
562 2024. Neurotransmitter classification from electron microscopy images at synaptic sites
563 in Drosophila melanogaster. *Cell* **187**:2574-2594.e23. doi:10.1016/j.cell.2024.03.016

564 Ehmann N, Linde S van de, Alon A, Ljaschenko D, Keung XZ, Holm T, Rings A,
565 DiAntonio A, Hallermann S, Ashery U, Heckmann M, Sauer M, Kittel RJ. 2014.
566 Quantitative super-resolution imaging of Bruchpilot distinguishes active zone states. *Nat*
567 *Commun* **5**:4650. doi:10.1038/ncomms5650

568 Fernández MP, Berni J, Ceriani MF. 2008. Circadian Remodeling of Neuronal Circuits
569 Involved in Rhythmic Behavior. *PLoS Biol* **6**:e69. doi:10.1371/journal.pbio.0060069

570 Fouquet W, Owald D, Wichmann C, Mertel S, Depner H, Dyba M, Hallermann S, Kittel
571 RJ, Eimer S, Sigrist SJ. 2009. Maturation of active zone assembly by Drosophila
572 Bruchpilot. *J Cell Biol* **186**:129–145. doi:10.1083/jcb.200812150

573 Gao R, Asano SM, Upadhyayula S, Pisarev I, Milkie DE, Liu T-L, Singh V, Graves A,
574 Huynh GH, Zhao Y, Bogovic J, Colonell J, Ott CM, Zugates C, Tappan S, Rodriguez A,
575 Mosaliganti KR, Sheu S-H, Pasolli HA, Pang S, Xu CS, Megason SG, Hess H,
576 Lippincott-Schwartz J, Hantman A, Rubin GM, Kirchhausen T, Saalfeld S, Aso Y,
577 Boyden ES, Betzig E. 2019. Cortical column and whole-brain imaging with molecular
578 contrast and nanoscale resolution. *Science* **363**. doi:10.1126/science.aau8302

579 Ghelani T, Escher M, Thomas U, Esch K, Lützkendorf J, Depner H, Maglione M, Parutto
580 P, Gratz S, Matkovic-Rachid T, Ryglewski S, Walter AM, Holcman D, Giles KO, Heine
581 M, Sigrist SJ. 2023. Interactive nanocluster compaction of the ELKS scaffold and
582 Cacophony Ca2+ channels drives sustained active zone potentiation. *Sci Adv*
583 **9**:eade7804. doi:10.1126/sciadv.ade7804

584 Gilestro GF, Tononi G, Cirelli C. 2009. Widespread Changes in Synaptic Markers as a
585 Function of Sleep and Wakefulness in Drosophila. *Science* **324**:109–112.
586 doi:10.1126/science.1166673

587 Graf ER, Daniels RW, Burgess RW, Schwarz TL, DiAntonio A. 2009. Rab3 Dynamically
588 Controls Protein Composition at Active Zones. *Neuron* **64**:663–677.
589 doi:10.1016/j.neuron.2009.11.002

590 Gratz SJ, Goel P, Bruckner JJ, Hernandez RX, Khateeb K, Macleod GT, Dickman D,
591 O'Connor-Giles KM. 2019. Endogenous tagging reveals differential regulation of Ca2+
592 channels at single AZs during presynaptic homeostatic potentiation and depression. *J*
593 *Neurosci* **39**:3068–18. doi:10.1523/jneurosci.3068-18.2019

594 Haase R, Royer LA, Steinbach P, Schmidt D, Dibrov A, Schmidt U, Weigert M, Maghelli
595 N, Tomancak P, Jug F, Myers EW. 2020. CLIJ: GPU-accelerated image processing for
596 everyone. *Nat Methods* **17**:5–6. doi:10.1038/s41592-019-0650-1

597 Hallermann S, Kittel RJ, Wichmann C, Weyhersmüller A, Fouquet W, Mertel S, Owald D,
598 Eimer S, Depner H, Schwärzel M, Sigrist SJ, Heckmann M. 2010. Naked Dense Bodies
599 Provoke Depression. *J Neurosci* **30**:14340–14345. doi:10.1523/jneurosci.2495-10.2010

600 Haynes PR, Christmann BL, Griffith LC. 2015. A single pair of neurons links sleep to
601 memory consolidation in Drosophila melanogaster. *eLife* **4**:e03868.
602 doi:10.7554/elife.03868

603 Hiramatsu S, Saito K, Kondo S, Katow H, Yamagata N, Wu C-F, Tanimoto H. 2024. Cell-
604 type-specific fluorescent tagging of endogenous target proteins reveals synaptic
605 enrichment and dynamic regulations of dopamine receptors. doi:10.7554/elife.98358.1

606 Huang S, Piao C, Beuschel CB, Götz T, Sigrist SJ. 2020. Presynaptic Active Zone
607 Plasticity Encodes Sleep Need in Drosophila. *Curr Biol* **30**:1077-1091.e5.
608 doi:10.1016/j.cub.2020.01.019

609 Jenett A, Rubin GM, Ngo T-TB, Shepherd D, Murphy C, Dionne H, Pfeiffer BD, Cavallaro
610 A, Hall D, Jeter J, Iyer N, Fetter D, Hausenfluck JH, Peng H, Trautman ET, Svirskas
611 RR, Myers EW, Iwinski ZR, Aso Y, DePasquale GM, Enos A, Hulamm P, Lam SCB, Li
612 H-H, Laverty TR, Long F, Qu L, Murphy SD, Rokicki K, Safford T, Shaw K, Simpson
613 JH, Sowell A, Tae S, Yu Y, Zugates CT. 2012. A GAL4-Driver Line Resource for
614 Drosophila Neurobiology. *Cell Rep* **2**:991–1001. doi:10.1016/j.celrep.2012.09.011

615 Kamiyama D, Sekine S, Barsi-Rhyne B, Hu J, Chen B, Gilbert LA, Ishikawa H, Leonetti
616 MD, Marshall WF, Weissman JS, Huang B. 2016. Versatile protein tagging in cells with
617 split fluorescent protein. *Nat Commun* **7**:11046. doi:10.1038/ncomms11046

618 Kawasaki F, Zou B, Xu X, Ordway RW. 2004. Active Zone Localization of Presynaptic
619 Calcium Channels Encoded by the cacophony Locus of Drosophila. *J Neurosci* **24**:282–
620 285. doi:10.1523/jneurosci.3553-03.2004

621 Ke M-T, Nakai Y, Fujimoto S, Takayama R, Yoshida S, Kitajima TS, Sato M, Imai T.
622 2016. Super-Resolution Mapping of Neuronal Circuitry With an Index-Optimized
623 Clearing Agent. *Cell Reports* **14**:2718–2732. doi:10.1016/j.celrep.2016.02.057

624 Keene AC, Krashes MJ, Leung B, Bernard JA, Waddell S. 2006. Drosophila Dorsal Paired
625 Medial Neurons Provide a General Mechanism for Memory Consolidation. *Curr Biol*
626 **16**:1524–1530. doi:10.1016/j.cub.2006.06.022

627 Keene AC, Stratmann M, Keller A, Perrat PN, Vosshall LB, Waddell S. 2004. Diverse
628 Odor-Conditioned Memories Require Uniquely Timed Dorsal Paired Medial Neuron
629 Output. *Neuron* **44**:521–533. doi:10.1016/j.neuron.2004.10.006

630 Kittel RJ, Wichmann C, Rasse TM, Fouquet W, Schmidt M, Schmid A, Wagh DA, Pawlu
631 C, Kellner RR, Willig KI, Hell SW, Buchner E, Heckmann M, Sigrist SJ. 2006.
632 Bruchpilot Promotes Active Zone Assembly, Ca^{2+} Channel Clustering, and Vesicle
633 Release. *Science* **312**:1051–1054. doi:10.1126/science.1126308

634 Kondo S, Takahashi T, Yamagata N, Imanishi Y, Katow H, Hiramatsu S, Lynn K, Abe A,
635 Kumaraswamy A, Tanimoto H. 2020. Neurochemical Organization of the Drosophila
636 Brain Visualized by Endogenously Tagged Neurotransmitter Receptors. *Cell Reports*
637 **30**:284-297.e5. doi:10.1016/j.celrep.2019.12.018

638 Kondo S, Ueda R. 2013. Highly Improved Gene Targeting by Germline-Specific Cas9
639 Expression in Drosophila. *Genetics* **195**:715–721. doi:10.1534/genetics.113.156737

640 Kremer MC, Christiansen F, Leiss F, Paehler M, Knapek S, Andlauer TFM, Förstner F,
641 Kloppenburg P, Sigrist SJ, Tavosanis G. 2010. Structural Long-Term Changes at
642 Mushroom Body Input Synapses. *Curr Biol* **20**:1938–1944.
643 doi:10.1016/j.cub.2010.09.060

644 Lee P-T, Lin H-W, Chang Y-H, Fu T-F, Dubnau J, Hirsh J, Lee T, Chiang A-S. 2011.
645 Serotonin–mushroom body circuit modulating the formation of anesthesia-resistant
646 memory in Drosophila. *Proc Natl Acad Sci* **108**:13794–13799.
647 doi:10.1073/pnas.1019483108

648 Lin AC, Bygrave AM, Calignon A de, Lee T, Miesenböck G. 2014. Sparse, decorrelated
649 odor coding in the mushroom body enhances learned odor discrimination. *Nat Neurosci*
650 **17**:559–568. doi:10.1038/nn.3660

651 Liu C, Plaçais P-Y, Yamagata N, Pfeiffer BD, Aso Y, Friedrich AB, Siwanowicz I, Rubin
652 GM, Preat T, Tanimoto H. 2012. A subset of dopamine neurons signals reward for
653 odour memory in Drosophila. *Nature* **488**:512–516. doi:10.1038/nature11304

654 Liu X, Davis RL. 2009. The GABAergic anterior paired lateral neuron suppresses and is
655 suppressed by olfactory learning. *Nat Neurosci* **12**:53–59. doi:10.1038/nn.2235

656 Matkovic T, Siebert M, Knoche E, Depner H, Mertel S, Owald D, Schmidt M, Thomas U,
657 Sickmann A, Kamin D, Hell SW, Bürger J, Hollmann C, Mielke T, Wichmann C,
658 Sigrist SJ. 2013. The Bruchpilot cytomatrix determines the size of the readily releasable
659 pool of synaptic vesicles. *J Cell Biol* **202**:667–683. doi:10.1083/jcb.201301072

660 Mosca TJ, Luo L. 2014. Synaptic organization of the Drosophila antennal lobe and its
661 regulation by the Teneurins. *eLife* **3**:e03726. doi:10.7554/elife.03726

662 Mrestani A, Pauli M, Kollmannsberger P, Repp F, Kittel RJ, Eilers J, Doose S, Sauer M,
663 Sirén A-L, Heckmann M, Paul MM. 2021. Active zone compaction correlates with
664 presynaptic homeostatic potentiation. *Cell Rep* **37**:109770.
665 doi:10.1016/j.celrep.2021.109770

666 Newman ZL, Bakshinskaya D, Schultz R, Kenny SJ, Moon S, Aghi K, Stanley C, Marnani
667 N, Li R, Bleier J, Xu K, Isacoff EY. 2022. Determinants of synapse diversity revealed
668 by super-resolution quantal transmission and active zone imaging. *Nat Commun* **13**:229.
669 doi:10.1038/s41467-021-27815-2

670 Ollion J, Cochennec J, Loll F, Escudé C, Boudier T. 2013. TANGO: a generic tool for
671 high-throughput 3D image analysis for studying nuclear organization. *Bioinformatics*
672 **29**:1840–1841. doi:10.1093/bioinformatics/btt276

673 Paul MM, Pauli M, Ehmann N, Hallermann S, Sauer M, Kittel RJ, Heckmann M. 2015.
674 Bruchpilot and Synaptotagmin collaborate to drive rapid glutamate release and active
675 zone differentiation. *Front Cell Neurosci* **9**:29. doi:10.3389/fncel.2015.00029

676 Perisse E, Yin Y, Lin AC, Lin S, Huetteroth W, Waddell S. 2013. Different Kenyon Cell
677 Populations Drive Learned Approach and Avoidance in Drosophila. *Neuron* **79**:945–
678 956. doi:10.1016/j.neuron.2013.07.045

679 Perkins LA, Holderbaum L, Tao R, Hu Y, Sopko R, McCall K, Yang-Zhou D, Flockhart I,
680 Binari R, Shim H-S, Miller A, Housden A, Foos M, Randkelv S, Kelley C, Namgyal P,
681 Villalta C, Liu L-P, Jiang X, Huan-Huan Q, Wang X, Fujiyama A, Toyoda A, Ayers K,
682 Blum A, Czech B, Neumuller R, Yan D, Cavallaro A, Hibbard K, Hall D, Cooley L,
683 Hannon GJ, Lehmann R, Parks A, Mohr SE, Ueda R, Kondo S, Ni J-Q, Perrimon N.

684 2015. The Transgenic RNAi Project at Harvard Medical School: Resources and
685 Validation. *Genetics* **201**:843–852. doi:10.1534/genetics.115.180208

686 Pfeiffer BD, Jenett A, Hammonds AS, Ngo T-TB, Misra S, Murphy C, Scully A, Carlson
687 JW, Wan KH, Laverty TR, Mungall C, Svirskas R, Kadonaga JT, Doe CQ, Eisen MB,
688 Celniker SE, Rubin GM. 2008. Tools for neuroanatomy and neurogenetics in
689 Drosophila. *Proc Natl Acad Sci* **105**:9715–9720. doi:10.1073/pnas.0803697105

690 Pitman JL, Huetteroth W, Burke CJ, Krashes MJ, Lai S-L, Lee T, Waddell S. 2011. A Pair
691 of Inhibitory Neurons Are Required to Sustain Labile Memory in the Drosophila
692 Mushroom Body. *Curr Biol* **21**:855–861. doi:10.1016/j.cub.2011.03.069

693 Rhea JM, Wegener C, Bender M. 2010. The Proprotein Convertase Encoded by
694 amontillado (amon) Is Required in Drosophila Corpora Cardiaca Endocrine Cells
695 Producing the Glucose Regulatory Hormone AKH. *PLoS Genet* **6**:e1000967.
696 doi:10.1371/journal.pgen.1000967

697 Sachidanandan D, Aravamudhan A, Mrestani A, Nerlich J, Lamberty M, Hasenauer N,
698 Ehmann N, Pauls D, Seubert T, Maiellaro I, Selcho M, Heckmann M, Hallermann S,
699 Kittel RJ. 2023. Rab3 mediates cyclic AMP-dependent presynaptic plasticity and
700 olfactory learning. *bioRxiv* 2023.12.21.572589. doi:10.1101/2023.12.21.572589

701 Sachse S, Rueckert E, Keller A, Okada R, Tanaka NK, Ito K, Vosshall LB. 2007. Activity-
702 Dependent Plasticity in an Olfactory Circuit. *Neuron* **56**:838–850.
703 doi:10.1016/j.neuron.2007.10.035

704 Sage D, Donati L, Soulez F, Fortun D, Schmit G, Seitz A, Guiet R, Vonesch C, Unser M.
705 2017. DeconvolutionLab2: An open-source software for deconvolution microscopy.
706 *Methods* **115**:28–41. doi:10.1016/j.ymeth.2016.12.015

707 Saito K, Kanno M, Tanimoto H, Ichinose T. 2025. Ecdysteroid-DopEcR signaling in
708 neuronal and midgut cells mediates toxin avoidance and detoxification in Drosophila.
709 *Curr Biol* **35**:3418-3428.e4. doi:10.1016/j.cub.2025.06.023

710 Scheffer LK, Xu CS, Januszewski M, Lu Z, Takemura Shin-ya, Hayworth KJ, Huang GB,
711 Shinomiya K, Maitlin-Shepard J, Berg S, Clements J, Hubbard PM, Katz WT, Umayam
712 L, Zhao T, Ackerman D, Blakely T, Bogovic J, Dolafi T, Kainmueller D, Kawase T,
713 Khairy KA, Leavitt L, Li PH, Lindsey L, Neubarth N, Olbris DJ, Otsuna H, Trautman
714 ET, Ito M, Bates AS, Goldammer J, Wolff T, Svirskas R, Schlegel P, Neace E, Knecht
715 CJ, Alvarado CX, Bailey DA, Ballinger S, Borycz JA, Canino BS, Cheatham N, Cook
716 M, Dreher M, Duclos O, Eubanks B, Fairbanks K, Finley S, Forknall N, Francis A,
717 Hopkins GP, Joyce EM, Kim S, Kirk NA, Kovalyak J, Lauchie SA, Lohff A,
718 Maldonado C, Manley EA, McLin S, Mooney C, Ndama M, Ogundeyi O, Okeoma N,

Ordish C, Padilla N, Patrick CM, Paterson T, Phillips EE, Phillips EM, Rampally N, Ribeiro C, Robertson MK, Rymer JT, Ryan SM, Sammons M, Scott AK, Scott AL, Shinomiya A, Smith C, Smith K, Smith NL, Sobeski MA, Suleiman A, Swift J, Takemura Satoko, Talebi I, Tarnogorska D, Tenshaw E, Tokhi T, Walsh JJ, Yang T, Horne JA, Li F, Parekh R, Rivlin PK, Jayaraman V, Costa M, Jefferis GS, Ito K, Saalfeld S, George R, Meinertzhagen IA, Rubin GM, Hess HF, Jain V, Plaza SM. 2020. A connectome and analysis of the adult Drosophila central brain. *Elife* **9**:e57443. doi:10.7554/elife.57443

Schlegel P, Yin Y, Bates AS, Dorkenwald S, Eichler K, Brooks P, Han DS, Gkantia M, Santos Marcia dos, Munnelly EJ, Badalamente G, Capdevila LS, Sane VA, Fragniere AMC, Kiassat L, Pleijzier MW, Stürner T, Tamimi IFM, Dunne CR, Salgarella I, Javier A, Fang S, Perlman E, Kazimiers T, Jagannathan SR, Matsliah A, Sterling AR, Yu Szi-chieh, McKellar CE, Schlegel P, Yin Y, Dorkenwald S, Eichler K, Brooks P, Gkantia M, Badalamente G, Capdevila LS, Tamimi IFM, Salgarella I, Javier A, Fang S, Perlman E, Matsliah A, Yu Szi-chieh, McKellar CE, Kruk K, Bland D, Lenizo Z, Burke AT, Willie KP, Bates AS, Serafetinidis N, Hadjerol N, Willie R, Silverman B, Ocho JA, Bañez J, Candilada RA, Gager J, Kristiansen A, Panes N, Yadav A, Tancontian R, Serona S, Dolorosa JI, Vinson KJ, Garner D, Salem R, Dagohoy A, Skelton J, Lopez M, Stocks T, Pandey A, Akiatan DJ, Hebditch J, David C, Sapkal D, Monungolh SM, Sane V, Pielago ML, Albero M, Laude J, Santos Márcia dos, Deutsch D, Vohra Z, Wang K, Gogo AM, Kind E, Mandahay AJ, Martinez C, Asis JD, Nair C, Patel D, Manaytay M, Lim CA, Ampo PL, Pantujan MD, Bautista D, Rana R, Seguido J, Parmar B, Saguimpa JC, Moore M, Pleijzier MW, Larson M, Hsu J, Joshi I, Kakadiya D, Braun A, Pilapil C, Parmar K, Vanderbeck Q, Dunne C, Munnelly E, Kang CH, Lörsch L, Lee J, Kmecova L, Sancer G, Baker C, Joroff J, Calle S, Patel Y, Sato O, Salocot J, Salman F, Molina-Obando S, Bui M, Lichtenberger M, Tamboboy E, Molloy K, Santana-Cruz AE, Hernandez A, Yu Seongbong, Sorek M, Diwan A, Patel M, Aiken TR, Morejohn S, Koskela S, Yang T, Lehmann D, Chojetzki J, Sisodiya S, Koolman S, Shiu PK, Cho S, Bast A, Reicher B, Blanquart M, Houghton L, Choi H, Ioannidou M, Collie M, Eckhardt J, Gorko B, Guo L, Zheng Z, Poh A, Lin M, Taisz I, Murfin W, Díez ÁS, Reinhard N, Gibb P, Patel N, Kumar S, Yun M, Wang M, Jones D, Encarnacion-Rivera L, Oswald A, Jadia A, Erginkaya M, Drummond N, Walter L, Tastekin I, Zhong X, Mabuchi Y, Santiago FJF, Verma U, Byrne N, Kunze E, Crahan T, Margossian R, Kim H, Georgiev I, Szorenyi F, Adachi A, Bargeron B, Stürner T, Demarest D, Gür B, Becker AN, Turnbull R, Morren A, Sandoval A, Moreno-Sanchez A, Pacheco DA, Samara E, Croke H, Thomson A, Laughland C, Dutta SB, Antón PGA de, Huang B, Pujols P, Haber I, González-Segarra A, Lin A, Choe DT, Lukyanova V, Mancini N, Liu Z, Okubo T, Flynn MA, Vitelli G, Laturney M, Li F, Cao S, Manyari-Diaz C, Yim H, Le AD, Maier K, Yu Seungyun, Nam Y, Bąba D, Abusaif A, Francis A, Gayk J, Huntress SS, Barajas R, Kim M, Cui X, Sterling AR, Sterne GR, Li A, Park K, Dempsey G, Mathew A, Kim Jinseong, Kim T, Wu G, Dhawan S, Brotas M, Zhang C, Bailey S, Toro AD, Lee K, Macrina T, Schneider-Mizell C, Popovych S, Ogedengbe O, Yang R, Halageri A, Silversmith W, Gerhard S, Champion A, Eckstein N, Ih D, Kemnitz N, Castro M, Jia Z,

762 Wu J, Mitchell E, Nehoran B, Mu S, Bae JA, Lu R, Morey R, Kuehner K, Brittain D,
763 Jordan CS, Anderson DJ, Behnia R, Bidaye SS, Borst A, Chiappe E, Collman F,
764 Colodner KJ, Dacks A, Dickson B, Funke J, Garcia D, Hampel S, Hartenstein V, Hassan
765 B, Helfrich-Forster C, Huetteroth W, Kim Jinseop, Kim SS, Kim Y-J, Kwon JY, Lee W-
766 C, Linneweber GA, Maimon G, Mann R, Noselli S, Pankratz M, Prieto-Godino L, Read
767 J, Reiser M, Reyn K von, Ribeiro C, Scott K, Seeds AM, Selcho M, Silies M, Simpson
768 J, Waddell S, Wernet MF, Wilson RI, Wolf FW, Yao Z, Yapici N, Zandawala M, Costa
769 M, Seung HS, Murthy M, Bock DD, Jefferis GSXE, Costa M, Seung HS, Murthy M,
770 Hartenstein V, Bock DD, Jefferis GSXE. 2024. Whole-brain annotation and multi-
771 connectome cell typing of Drosophila. *Nature* **634**:139–152. doi:10.1038/s41586-024-
772 07686-5

773 Schlegel P, Yin Y, Bates AS, Dorkenwald S, Eichler K, Brooks P, Han DS, Gkantia M,
774 Santos M dos, Munnelly EJ, Badalamente G, Capdevila LS, Sane VA, Pleijzier MW,
775 Tamimi IFM, Dunne CR, Salgarella I, Javier A, Fang S, Perlman E, Kazimiers T,
776 Jagannathan SR, Matsliah A, Sterling AR, Yu S, McKellar CE, Consortium F, Costa M,
777 Seung HS, Murthy M, Hartenstein V, Bock DD, Jefferis GSXE. 2023. A consensus cell
778 type atlas from multiple connectomes reveals principles of circuit stereotypy and
779 variation. *bioRxiv* 2023.06.27.546055. doi:10.1101/2023.06.27.546055

780 Stocker RF, Heimbeck G, Gendre N, Belle JS de. 1997. Neuroblast ablation in Drosophila
781 P[GAL4] lines reveals origins of olfactory interneurons. *J Neurobiol* **32**:443–456.
782 doi:10.1002/(sici)1097-4695(199705)32:5<443::aid-neu1>3.0.co;2-5

783 Sugie A, Hakeda-Suzuki S, Suzuki E, Silies M, Shimozono M, Möhl C, Suzuki T,
784 Tavosanis G. 2015. Molecular Remodeling of the Presynaptic Active Zone of
785 Drosophila Photoreceptors via Activity-Dependent Feedback. *Neuron* **86**:711–725.
786 doi:10.1016/j.neuron.2015.03.046

787 Takemura Shin-ya, Hayworth KJ, Huang GB, Januszewski M, Lu Z, Marin EC, Preibisch
788 S, Xu CS, Bogovic J, Champion AS, Cheong HS, Costa M, Eichler K, Katz W, Knecht
789 C, Li F, Morris BJ, Ordish C, Rivlin PK, Schlegel P, Shinomiya K, Stürner T, Zhao T,
790 Badalamente G, Bailey D, Brooks P, Canino BS, Clements J, Cook M, Duclos O, Dunne
791 CR, Fairbanks K, Fang S, Finley-May S, Francis A, George R, Gkantia M, Harrington
792 K, Hopkins GP, Hsu J, Hubbard PM, Javier A, Kainmueller D, Korff W, Kovalyak J,
793 Krzemiński D, Lauchie SA, Lohff A, Maldonado C, Manley EA, Mooney C, Neace E,
794 Nichols M, Ogundeyi O, Okeoma N, Paterson T, Phillips E, Phillips EM, Ribeiro C,
795 Ryan SM, Rymer JT, Scott AK, Scott AL, Shepherd D, Shinomiya A, Smith C, Smith
796 N, Suleiman A, Takemura Satoko, Talebi I, Tamimi IF, Trautman ET, Umayam L,
797 Walsh JJ, Yang T, Rubin GM, Scheffer LK, Funke J, Saalfeld S, Hess HF, Plaza SM,
798 Card GM, Jefferis GS, Berg S. 2024. A Connectome of the Male Drosophila Ventral
799 Nerve Cord. doi:10.7554/elife.97769.1

800 Tirian L, Dickson BJ. 2017. The VT GAL4, LexA, and split-GAL4 driver line collections
801 for targeted expression in the Drosophila nervous system. *bioRxiv* 198648.
802 doi:10.1101/198648

803 Turrel O, Ramesh N, Escher MJF, Pooryasin A, Sigrist SJ. 2022. Transient active zone
804 remodeling in the Drosophila mushroom body supports memory. *Curr Biol*.
805 doi:10.1016/j.cub.2022.10.017

806 Vogt K, Schnaitmann C, Dylla KV, Knapek S, Aso Y, Rubin GM, Tanimoto H. 2014.
807 Shared mushroom body circuits underlie visual and olfactory memories in Drosophila.
808 *Elife* **3**:e02395. doi:10.7554/elife.02395

809 Waddell S, Armstrong JD, Kitamoto T, Kaiser K, Quinn WG. 2000. The amnesiac Gene
810 Product Is Expressed in Two Neurons in the Drosophila Brain that Are Critical for
811 Memory. *Cell* **103**:805–813. doi:10.1016/s0092-8674(00)00183-5

812 Wagh DA, Rasse TM, Asan E, Hofbauer A, Schwenkert I, Dürrbeck H, Buchner S,
813 Dabauvalle M-C, Schmidt M, Qin G, Wichmann C, Kittel R, Sigrist SJ, Buchner E.
814 2006. Bruchpilot, a Protein with Homology to ELKS/CAST, Is Required for Structural
815 Integrity and Function of Synaptic Active Zones in Drosophila. *Neuron* **49**:833–844.
816 doi:10.1016/j.neuron.2006.02.008

817 Wu C-L, Shih M-FM, Lee P-T, Chiang A-S. 2013. An Octopamine-Mushroom Body
818 Circuit Modulates the Formation of Anesthesia-Resistant Memory in Drosophila. *Curr*
819 *Biol* **23**:2346–2354. doi:10.1016/j.cub.2013.09.056

820 Wu H, Eno S, Jinnai K, Abe A, Saito K, Maekawa Y, Williams DW, Yamagata N, Kondo
821 S, Tanimoto H. 2025. Octopamine signaling regulates the intracellular pattern of the
822 presynaptic active zone scaffold within Drosophila mushroom body neurons. *PLOS Biol*
823 **23**:e3003449. doi:10.1371/journal.pbio.3003449

824 Yamagata N, Ezaki T, Takahashi T, Wu H, Tanimoto H. 2021. Presynaptic inhibition of
825 dopamine neurons controls optimistic bias. *Elife* **10**:e64907. doi:10.7554/elife.64907

826 Yamagata N, Ichinose T, Aso Y, Plaçais P-Y, Friedrich AB, Sima RJ, Preat T, Rubin GM,
827 Tanimoto H. 2015. Distinct dopamine neurons mediate reward signals for short- and
828 long-term memories. *Proc National Acad Sci* **112**:578–583.
829 doi:10.1073/pnas.1421930112

830 Yu D, Keene AC, Srivatsan A, Waddell S, Davis RL. 2005. Drosophila DPM Neurons
831 Form a Delayed and Branch-Specific Memory Trace after Olfactory Classical
832 Conditioning. *Cell* **123**:945–957. doi:10.1016/j.cell.2005.09.037

833 Zeng J, Li X, Zhang R, Lv M, Wang Y, Tan K, Xia X, Wan J, Jing M, Zhang X, Li Yu,
834 Yang Y, Wang L, Chu J, Li Yan, Li Yulong. 2023. Local 5-HT signaling bi-
835 directionally regulates the coincidence time window for associative learning. *Neuron*
836 **111**:1118-1135.e5. doi:10.1016/j.neuron.2022.12.034

837 Zhang X, Li Q, Wang L, Liu Z-J, Zhong Y. 2018. Active Protection: Learning-Activated
838 Raf/MAPK Activity Protects Labile Memory from Rac1-Independent Forgetting.
839 *Neuron* **98**:142-155.e4. doi:10.1016/j.neuron.2018.02.025

840 Zheng Z, Lauritzen JS, Perlman E, Robinson CG, Nichols M, Milkie D, Torrens O, Price J,
841 Fisher CB, Sharifi N, Calle-Schuler SA, Kmecova L, Ali IJ, Karsh B, Trautman ET,
842 Bogovic JA, Hanslovsky P, Jefferis GSXE, Kazhdan M, Khairy K, Saalfeld S, Fetter
843 RD, Bock DD. 2018. A Complete Electron Microscopy Volume of the Brain of Adult
844 Drosophila melanogaster. *Cell* **174**:730-743.e22. doi:10.1016/j.cell.2018.06.019

845

846 **Acknowledgments**

847 We thank all lab members of Tanimoto Lab at Tohoku University for valuable discussions.
848 We thank Dr. Yuki Tsukada at Keio University for crucial advice on Fiji-based image
849 analysis. We thank Vienna Drosophila Resource Center and Bloomington Drosophila Stock
850 Center for transgenic flies.

851

852 **Funding:**

853 Japan Science and Technology Agency JPMJSP2114 (HW)
854 Tohoku University Research Program 'Frontier Research in Duo' (HT)
855 Ministry of Education, Culture, Sports, Science and Technology 20H00519 (HT)
856 Ministry of Education, Culture, Sports, Science and Technology 22H05481 (HT)
857 Ministry of Education, Culture, Sports, Science and Technology 22KK0106 (HT)

858

859 **Author contributions:**

860 Conceptualization: HW, HT
861 Methodology: HW, YM, NY, SE, SK
862 Investigation: HW, YM, SE
863 Visualization: HW, SE

Resources: SK

Supervision: HW, NY, HT

Writing—original draft: HY, HT

Writing—review & editing: HW, SE, HT

Competing interests

Authors declare that they have no competing interests.

Data and materials availability

Further information and requests on resources and reagents should be directed to and will be fulfilled by the corresponding author, Dr. Hiromu Tanimoto (hiromut@m.tohoku.ac.jp). All data and codes needed to evaluate the conclusions in the paper are present in the paper.

Main figures

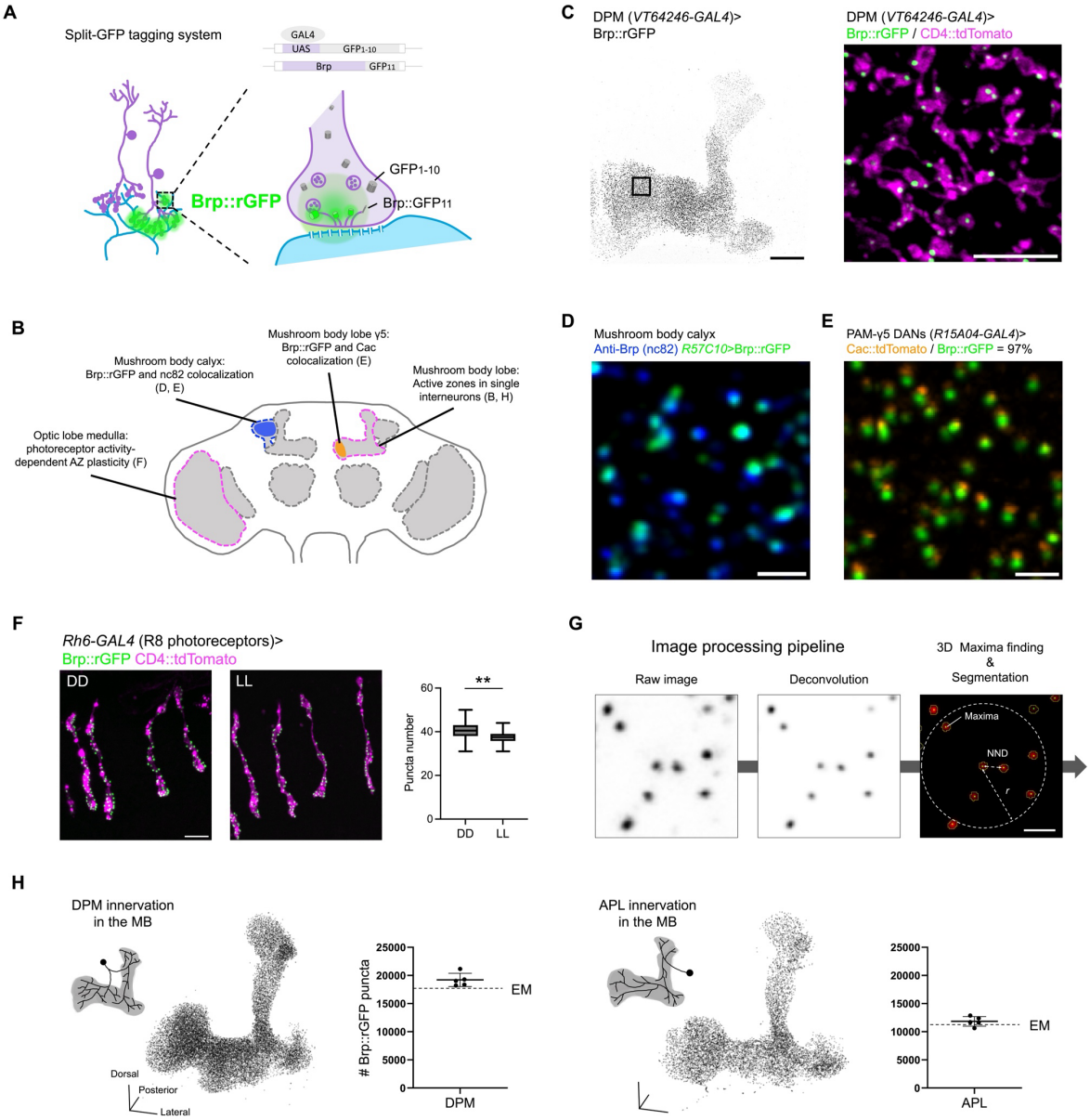

Figure 1 Spatial characterization of Brp::rGFP clusters at single-AZ level.

(**A**) Schematic of the split-GFP tagging strategy. The GFP_{11} fragment is inserted by CRISPR/Cas9 just prior to the stop codon of *brp*, while GFP_{1-10} is expressed in specific cell types via GAL4-UAS system.

882 (**B**) Brp::rGFP signals in DPM. The entire MB lobe structure is shown. The black box in
883 the left panel indicates the zoom-in area (right panel). GFP_{1-10} and CD4::tdTomato
884 (magenta) were co-expressed using *VT64246-GAL4*. Scale bar, 20 μm (left); 5 μm (right).
885 (**C**) Schematic showing brain regions and cell types analyzed in Figure 1C-F and H.
886 (**D**) Brp::rGFP (green) and anti-Brp immunostaining signals (blue) in the mushroom body
887 calyx. GFP_{1-10} was expressed using pan-neuronal driver *R57C10-GAL4*. Scale bar, 1 μm.
888 (**E**) Brp::rGFP (green) and Cac::tdTomato (orange) in PAM-γ5 dopamine neuron terminals.
889 GFP_{1-10} and Cac::tdTomato were co-expressed using *R15A04-GAL4.* Scale bar, 1 μm.
890 (**F**) Brp::rGFP (green) in R8 photoreceptors upon constant dark or light conditions. GFP_{1-10}
891 and CD4::TdTomato (magenta) were co-expressed using *Rh6-GAL4*. Brp::rGFP cluster
892 number of each R8 photoreceptor terminal in the medulla were quantified. n = 30 (3 brain
893 samples, 10 terminals from each brain). Welch's t test. Scale bar, 5 μm.
894 (**G**) Image processing pipeline. Raw images were processed with image deconvolution to
895 improve the signal quality. 3D maxima (green pixels) are detected for each Brp::rGFP
896 cluster. 3D ROIs are indicated by yellow circles. Nearest neighbor distance (NND), *r* is
897 defined as 3 × mean NND. Scale bar, 1 μm.
898 (**H**) Number of Brp::rGFP clusters detected in DPM and APL. The dashed lines indicate the
899 number of electron dense projections identified in the hemibrain connectome for DPM
900 (17530) and APL (10789) on the MB lobes and peduncle (Scheffer et al., 2020).
901 Schematics illustrate the innervation patterns of DPM and APL neurons. For both DPM and
902 APL, n = 5. Lower panels show the representative 3D reconstructions of Brp::rGFP clusters
903 in DPM and APL. Scale bars, 20 μm. Data were presented as mean ± s.e.m.
904

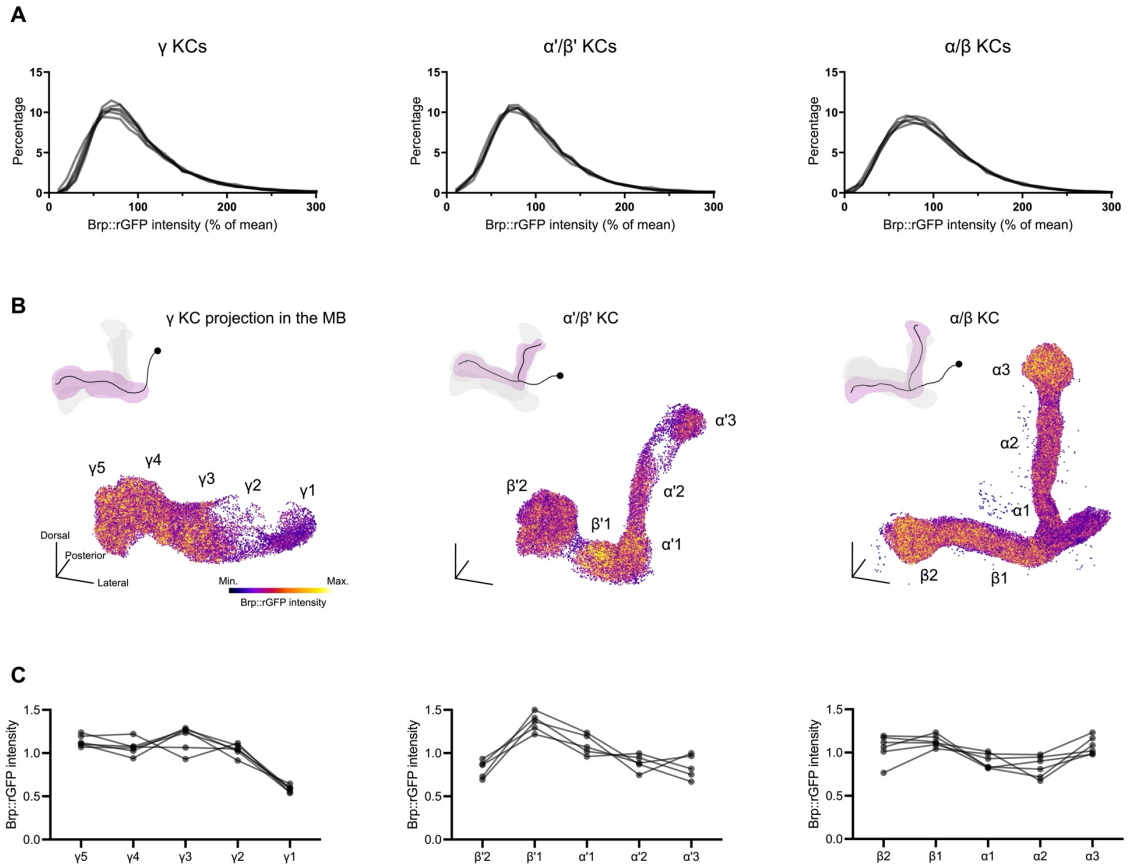

905

906 **Figure 2 Compartmentalized AZ structures of KCs.**

907 (**A**) Histograms of the signal intensity of individual Brp::rGFP clusters from three KC
908 subtypes. Values are normalized by the mean intensity in each data set (each sample). Each
909 line represents the histogram of one independent sample. γ KCs (*MB009B-GAL4*), n = 6;
910 α/β KCs (*MB370B-GAL4*), n = 5; α'/β' KCs (*MB008B-GAL4*), n = 5.

911 (**B**) 3D reconstructions of Brp::rGFP clusters in three KC subtypes, colored by the
912 Brp::rGFP intensity. The approximate locations of compartments are as indicated.
913 Schematics illustrate the innervation patterns of different KC subtypes. Min. and Max. were
914 set to represent the lowest and highest 5% of Brp::rGFP intensity value in the dataset
915 respectively. Scale bars, 20 μm.

916 (**C**) Signal intensity of Brp:rGFP clusters in each compartment. Brp::rGFP clusters were
917 quantified compartmentally. Medians in different compartments are showed as the ratio

918 against the average of five compartments in the corresponding KC subtype. Each line
919 represents one independent sample.
920

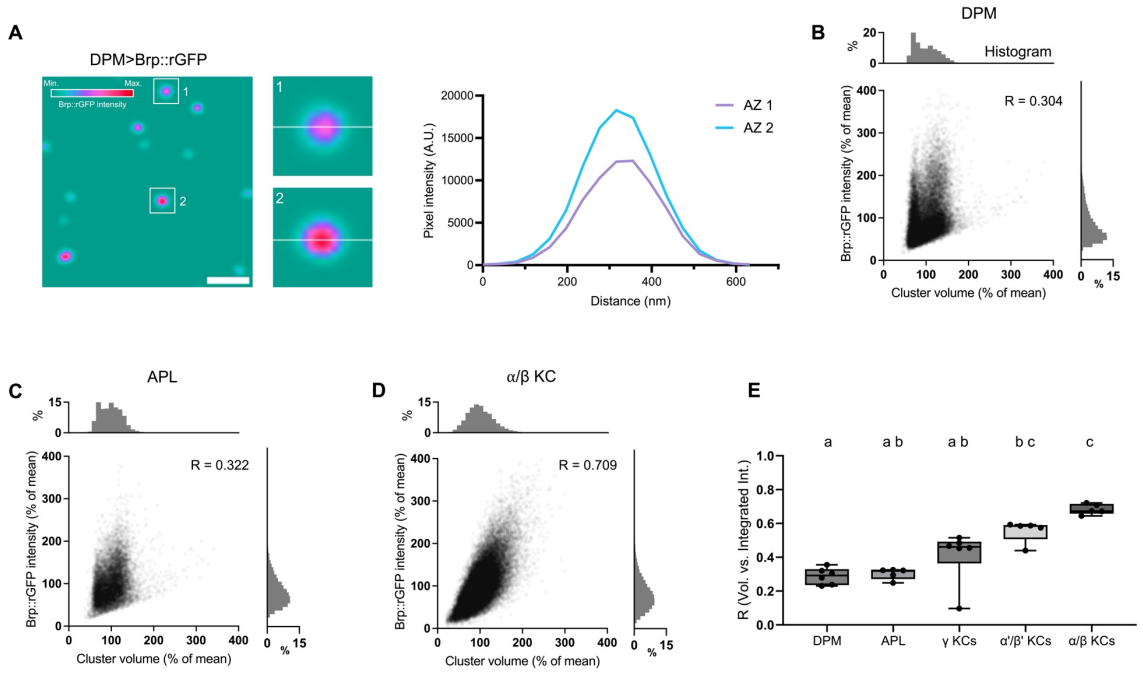

Figure 3 The variability of Brp::rGFP concentrations depends on cell type.

(**A**) Brp::rGFP clusters with distinct intensities but similar size in DPM. The left panel shows a cropped image of Brp::rGFP in DPM. White boxes indicate areas zoomed-in in panels 1 and 2. Transparent white lines in panels 1 and 2 show the lines on which the intensity profiles were plotted. Intensity profiles were plotted for AZ1 (magenta) and AZ2 (blue) respectively.

(**B-D**) Scatter plots showing the correlation between the Brp::rGFP intensity and cluster volume in DPM, APL and α/β KCs. Data of three representative samples were shown. Pearson correlation coefficient R were calculated for each sample.

(**E**) Correlations between the intensity and volume of Brp::rGFP clusters in different cell types. DPM (n = 6), APL (n = 5), γ KCs (n = 6, *MB009B-GAL4*), α'/β' KCs (n = 5, *MB370B-GAL4*), α/β KCs (n = 5, *MB008B-GAL4*). DPM vs. α'/β' KCs: P = 0.0253; DPM vs. α/β KCs: P = 0.0009; APL vs. α/β KCs: P = 0.0035; γ KCs vs. α/β KCs: P = 0.0418. Values marked with different lowercase letters represent significant difference ($P < 0.05$); Data were presented as box plots showing center (median), whiskers (Min. to Max.).

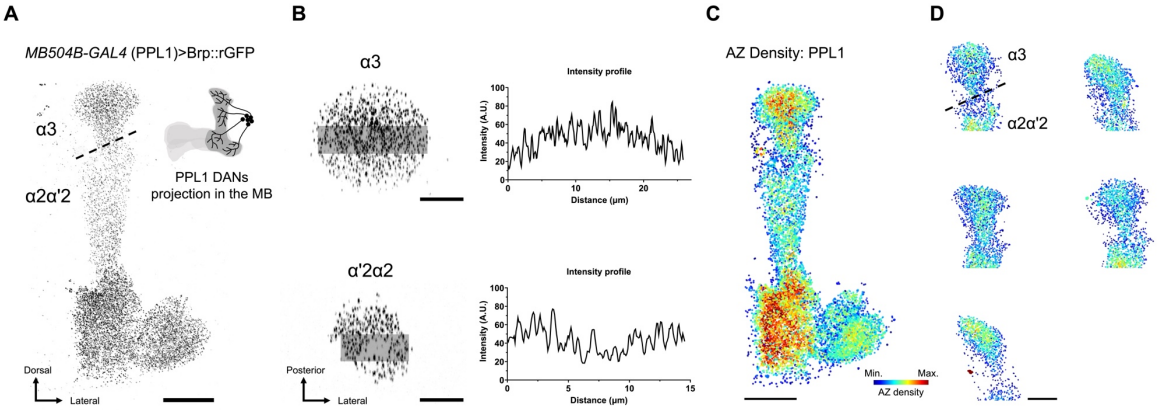

Figure 4 Stereotyped AZ distribution of PPL1-α3 DAN.

(**A**) Brp::rGFP in PPL1 DANs. UAS-GFP$_{1\text{-}10}$ was expressed using *MB504B-GAL4*. Dashed line marks the rough boundary between α3 and α2α'2 compartments. Schematic illustrates the innervation patterns of PPL1 DANs within the MB. Scale bar, 20 μm.

(**B**) Brp::rGFP intensity profiles of α3 and α2α'2 compartments. Left panels show the max-projection images of α3 and α2α'2 optical coronal sections. Transparent gray stripes indicate areas where intensity profiles are plotted in the right panels. Scale bars, 10 μm.

(**C**) 3D reconstruction colored by the AZ density in PPL-1 DANs. Color scale: Min. = 0, Max. = 40. Dashed line indicates the rough boundary between α3 and α2α'2 compartments. Scale bar, 20 μm.

(**D**) Stereotyped AZ distribution pattern in PPL1-α3 across individuals. 3D reconstructions show the AZ density across different brain samples. Scale bar, 20 μm.

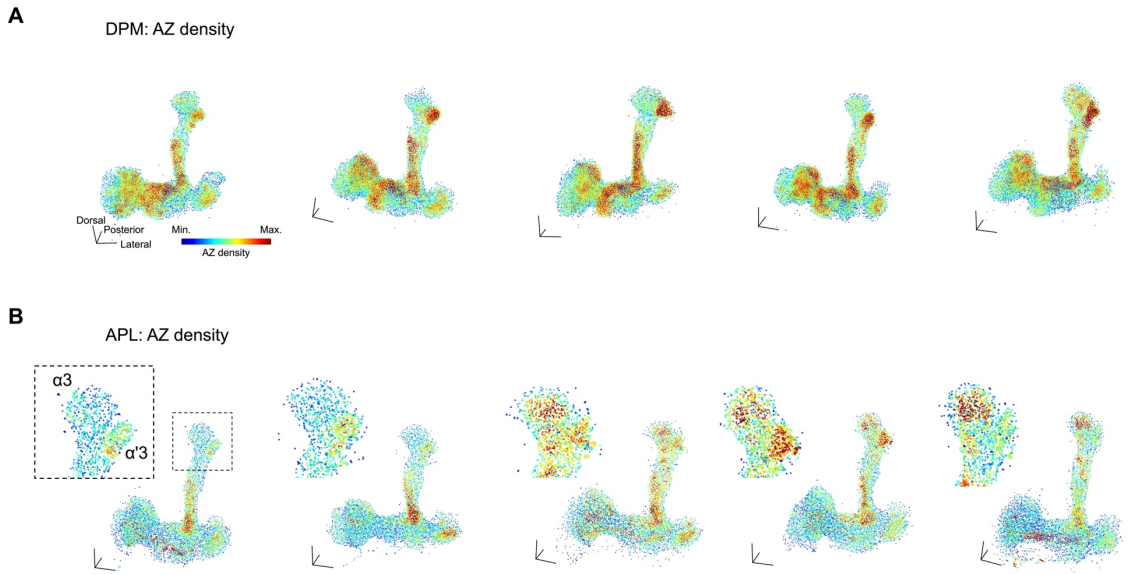

952

953 **Figure 5 Cell-type-specific stereotypy of AZ spatial distributions.**

954 (**A**) 3D reconstructions of Brp::rGFP clusters in DPMs, colored by AZ density. Color scale:

955 Min. = 0, Max. = 35. Black arrows indicate consistently high AZ density regions across

956 brain samples. Scale bars, 20 μm.

957 (**B**) 3D reconstructions of Brp::rGFP clusters in APLs, colored by AZ density. Color scale:

958 Min. = 0, Max. = 30. Black dashed square indicates the area zoomed in. APL

959 reconstructions are arranged from left to right according to the overall AZ density in α3.

960

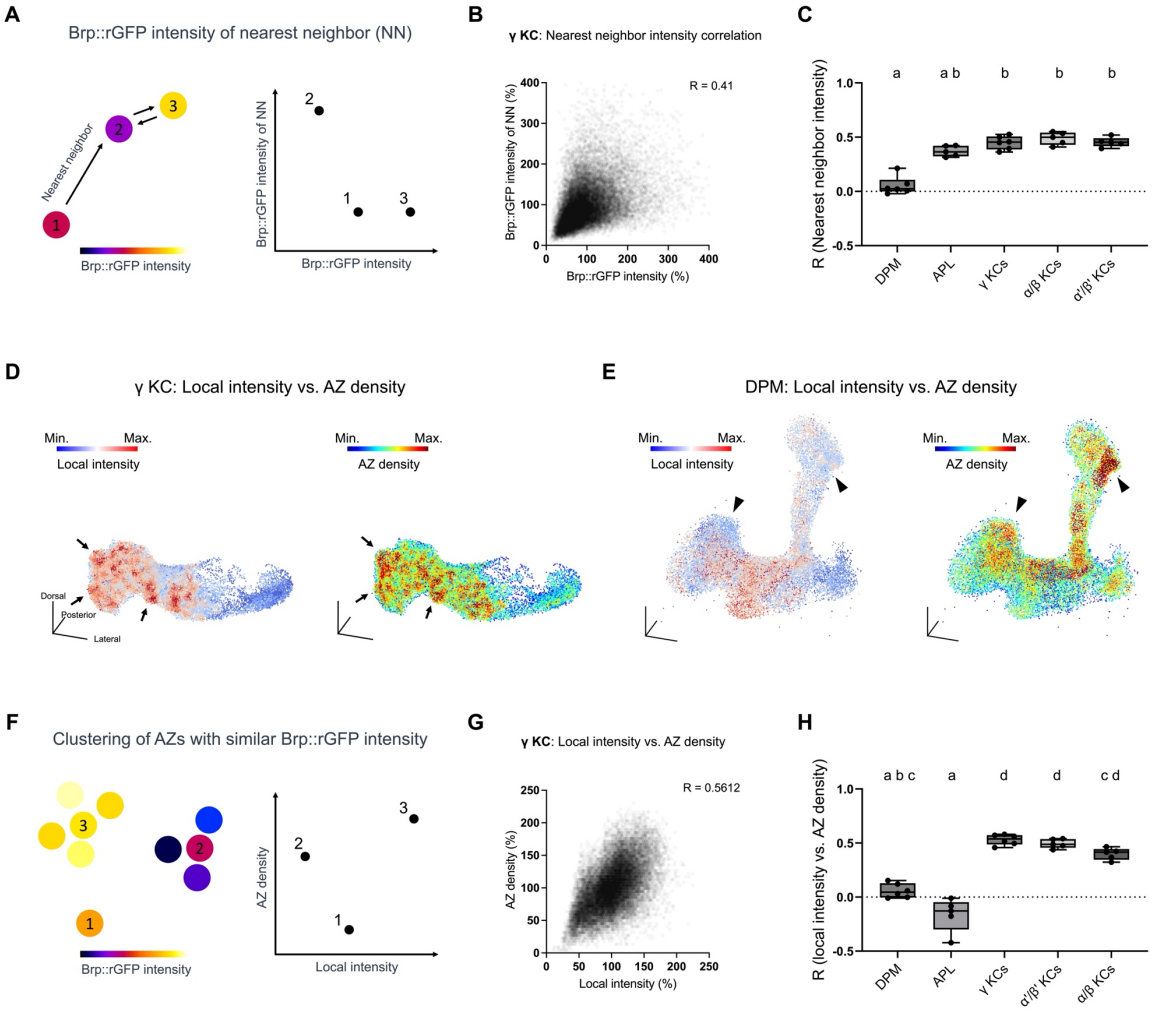

Figure 6 Local intensity analysis revealed sub-compartmental AZ structures.

(**A**) Brp::rGFP correlation analysis between nearest neighbors (NN). The intensity of a cluster is plotted on the x-axis and the intensity of its nearest neighbor is plotted on the y-axis. High correlation indicates nearest neighbors have similar Brp::rGFP intensity.

(**B**) Scatter plots showing the Brp::rGFP intensity correlation between nearest neighbors in a representative sample of γ KCs. Values were normalized to the mean. Pearson correlation coefficient R is shown.

(**C**) Correlation of Brp::rGFP intensities between nearest neighbor AZs in different cell types. Brp::rGFP intensities were log transformed. DPM vs. γ KCs: P = 0.0066; DPM vs. α'/β' KCs: P = 0.0027; DPM vs. α/β KCs: P = 0.0066; Scale bar: 1 μm.

(**D**) 3D reconstructions of Brp::rGFP clusters in a γ KC sample, colored by local intensity and AZ density. Black arrows indicate areas with both high local intensities and high AZ densities. Min. and Max. were set to represent the lowest and highest 5% in local intensity value respectively. Color scale of AZ density: Min. = 0 and Max = 35.

(**E**) 3D reconstructions of Brp::rGFP clusters in a DPM neuron, colored by local intensity and AZ density. Black triangle arrows indicate areas with high AZ densities but low local intensities. Min. and Max. are set to represent the lowest and highest 5% in local intensity value respectively. Color scale of AZ density: Min. = 0, Max. = 35.

(**F**) Correlation analysis between local intensity and AZ density. The local intensity of a cluster is plotted on the x-axis and its AZ density is plotted on the y-axis.

(**G**) Scatter plots showing the correlation between Brp::rGFP local intensity and AZ density in a representative sample of γ KCs. Values were normalized to the mean. Pearson correlation coefficient R is shown.

(**H**) Correlations between AZ density and local intensity in different cell types. DPM (n = 6), APL (n = 5), γ KCs (n = 6, *MB009B-GAL4*), α'/β' KCs (n = 5, *MB370B-GAL4*), α/β KCs (n = 5, *MB008B-GAL4*). DPM vs. γ KCs: P = 0.0171; DPM vs. α'/β' KCs: P = 0.0171; APL vs. γ KCs: P = 0.0014; APL vs. α'/β' KCs: P = 0.0014; APL vs. α/β KCs: P = 0.0171.

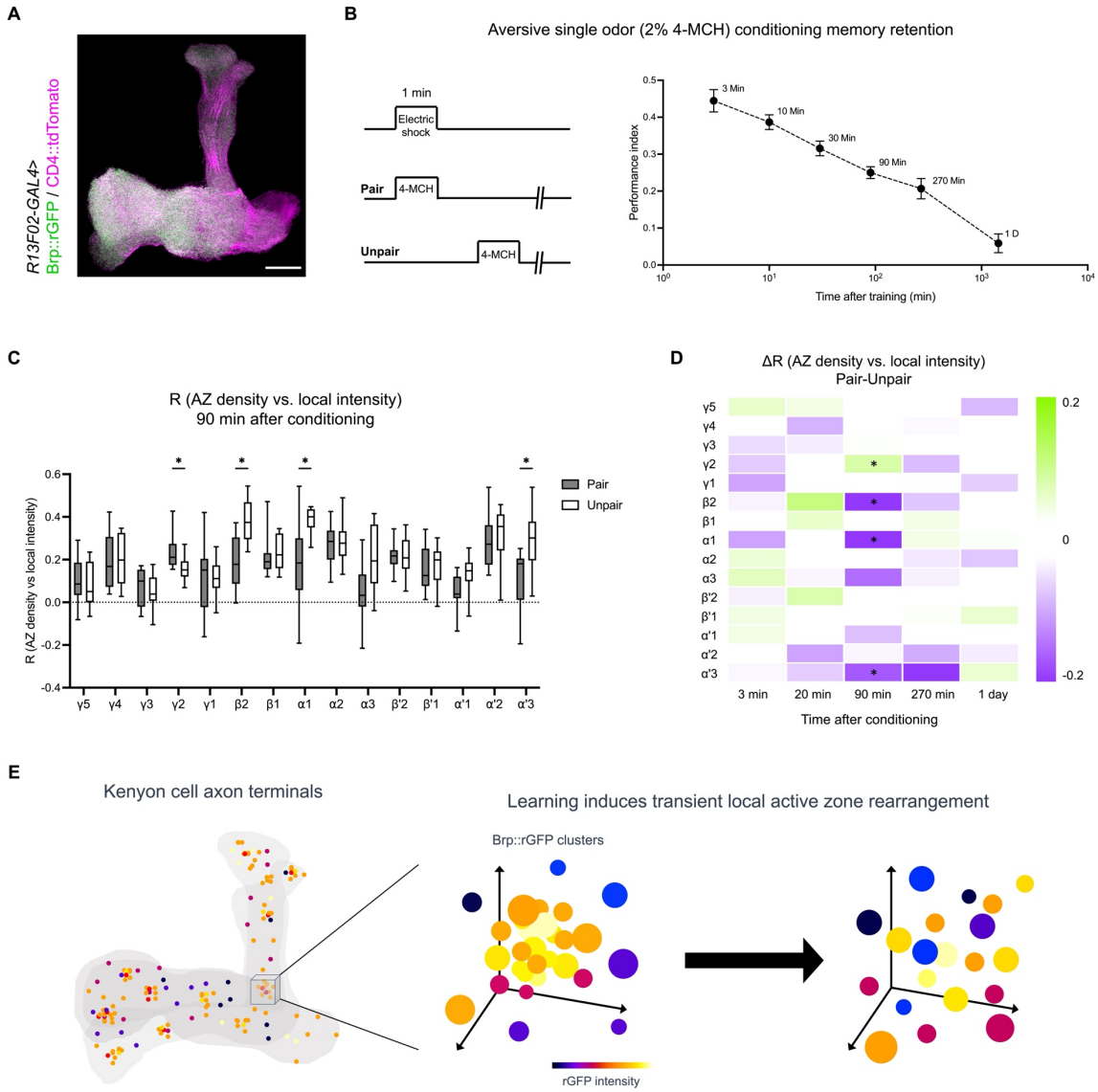

Figure 7 Associative conditioning re-organizes sub-compartmental active zone clusters.

(**A**) Brp::rGFP (green) and CD4::tdTomato cytoplasm membrane marker (magenta) in KCs, visualized by using *R13F02-GAL4*.

(**B**) Single odor conditioning induces long-lasting memory. Left panel, the experimental design of the aversive single odor conditioning. The paired group receives a concurrent presentation of 2% 4-MCH and 90 V electric shock. The unpaired group first receives the electric shock and then 4-MCH 1 min later. Right panel, preference of *Canton S* between

999 2% 4-MCH and paraffin oil at 3, 10, 30, 90, 270 minutes and 1 day after single odor
1000 conditioning. n = 8 for all groups. Error bars show S.E.M.
1001 (**C**) Correlation coefficient (AZ density vs. local intensity of individual Brp::rGFP clusters)
1002 of each compartment at 90 min after conditioning. Pair (n = 11) vs. Unpair (n = 12), γ2 (P =
1003 0.0261), β2 (P = 0.0060), α1 (P = 0.0026), α'3 (P = 0.0026).
1004 (**D**) Heatmap showing the difference of correlation coefficient (AZ density vs. local
1005 intensity of Brp::rGFP clusters) between the pair and unpair group at different time points
1006 after conditioning. The color indicates the difference and the asterisks in the compartments
1007 indicate the significant difference. For 3 min, Pair (n = 12), Unpair (n = 11); For 20 min,
1008 Pair (n = 12), Unpair (n = 11); For 90 min, Pair (n = 11) vs. Unpair (n = 12), P = 0.0247;
1009 For 270 min, Pair (n = 11), Unpair (n = 11), ; For 1 D, Pair (n = 12), Unpair (n = 9); For all
1010 results involved statistical comparison, only significant results are shown. Scale bars, 20
1011 μm. Mann-Whitney test with original False Discovery Rate method of Benjamini and
1012 Hochberg correction. *P<0.05. Data were presented as box plots showing centre (median),
1013 whiskers (Min. to Max.).
1014 (**E**) Schematics showing learning induced local AZ remodeling. Single odor aversive
1015 training transiently dismisses high Brp level – high AZ density hot spots in specific
1016 compartments of KC terminals.
1017

1018 **Figure supplements**

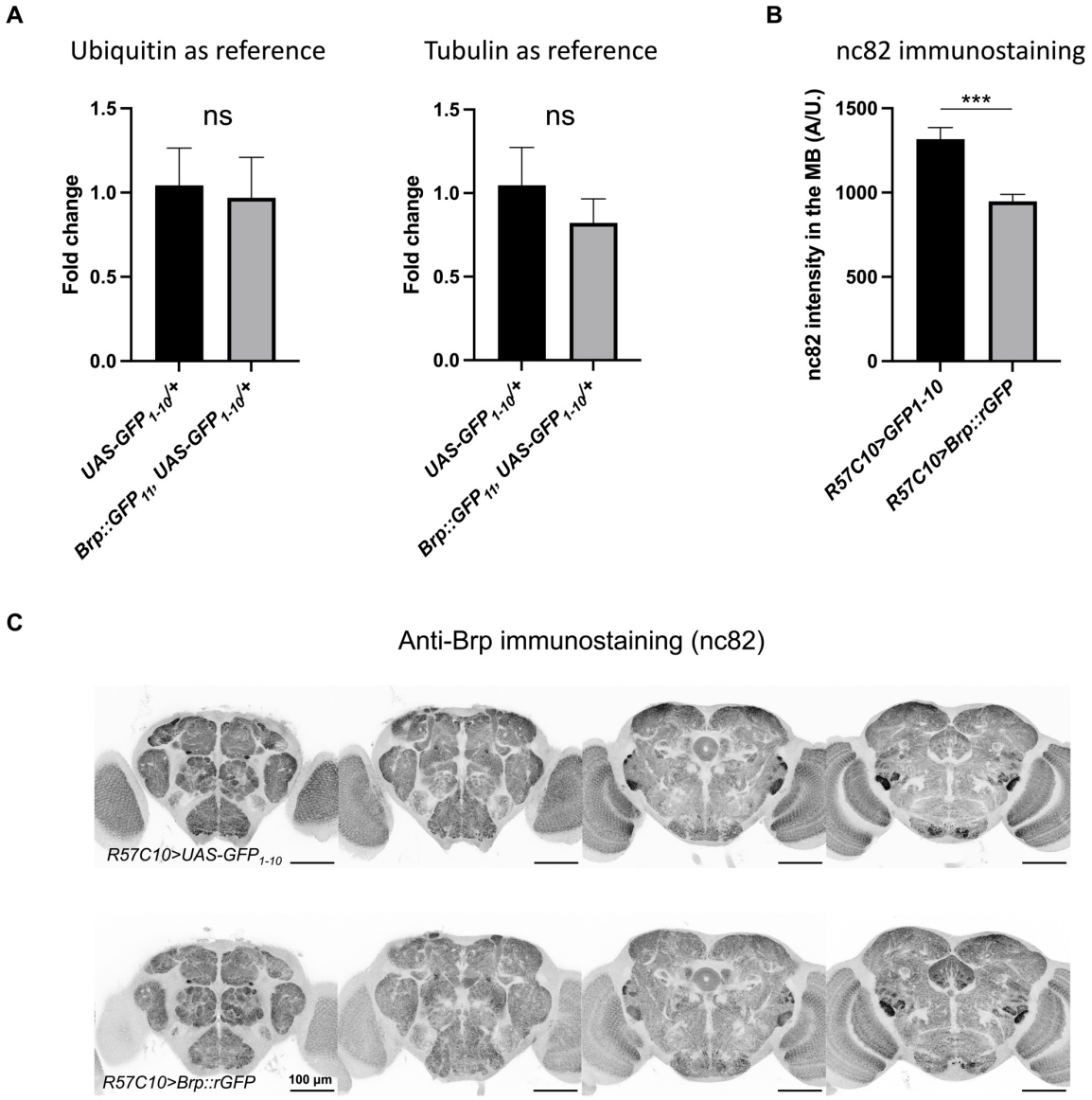

1019

1020 **Figure 1 – figure supplement 1 Split-GFP tagging does not affect Brp neuronal**
1021 **expression specificity and expression pattern in the brain.**
1022 (**A**) Fold change of *brp* mRNA level against reference genes, measured by qRT-PCR.
1023 mRNA of *Ubiquitin-5E* and *αTubulin84B* were used as the reference. n = 3 for all groups.
1024 Error bars show S.E.M. ns = non-significant. ***$p \leq 0.001$. Mann-Whitney test.

1025 (**B**) Anti-Brp (nc82) immunostaining signal in the MB of flies with or without GFP_{11}
1026 insertion. Both have expressions of GFP_{1-10} by *R57C10-GAL4*. n = 11 for both groups.
1027 Error bars show S.E.M.
1028 (**C**) Anti-Brp immunostaining of brains of flies with or without pan-neuronal Brp::rGFP
1029 tagging using *R57C10-GAL4.* Different planes of the image stack were shown. Scale bars,
1030 100 μm.
1031

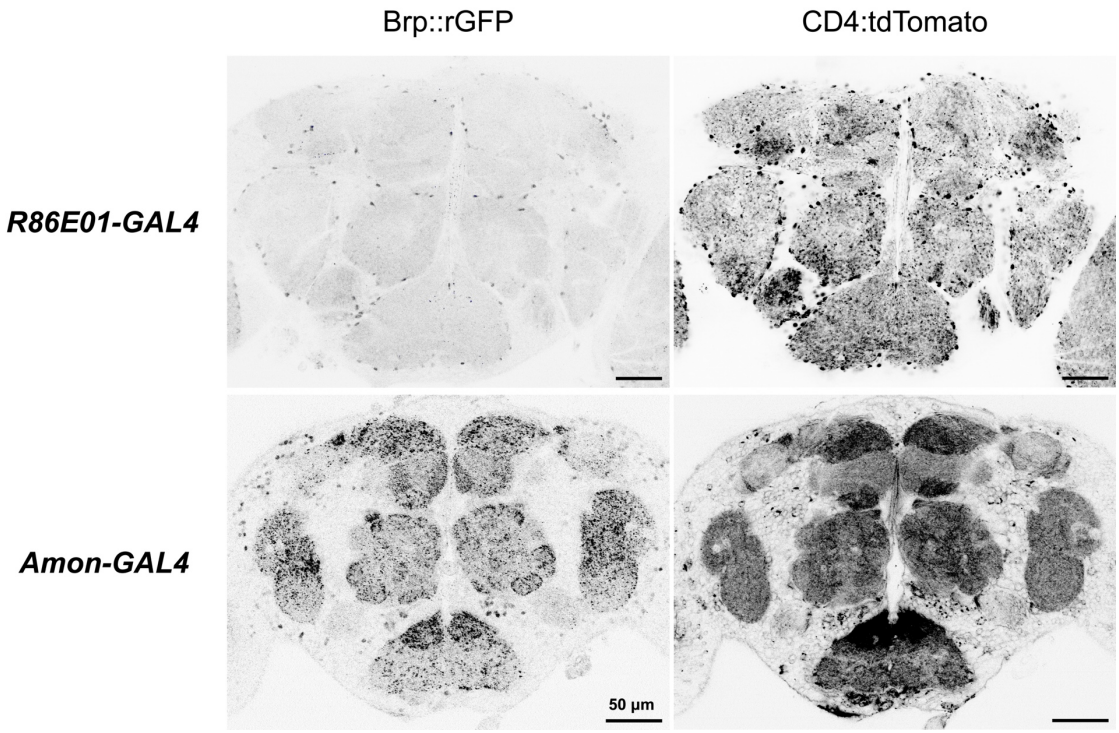

1032

1033 **Figure 1 – figure supplement 2 Neuron-specific assembly of Brp::rGFP.**

1034 Brp::rGFP and CD4::tdTomato were visualized in astrocyte-like glia using *R86E01-GAL4*,

1035 and in neuropeptide releasing neurons using *Amon-GAL4*, respectively. Images were

1036 acquired using comparable settings. Scale bars, 50 µm.

1037

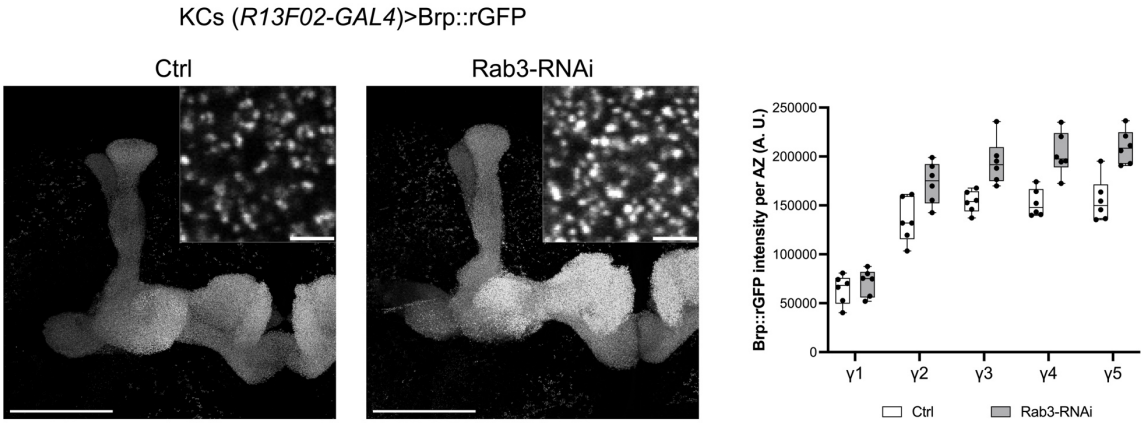

1038

1039 **Figure 1 – figure supplement 3 Rab3 knock-down in KCs increases Brp::rGFP**

1040 **intensity.**

1041 Rab3 was knocked-down in KCs using RNAi by *R13F02-GAL4*. The median of Brp::rGFP

1042 intensity of individual clusters was calculated for each γ compartment. n = 6 for both

1043 groups. Scale bars, 50 μm in the overview, 2 μm in the insets.

1044

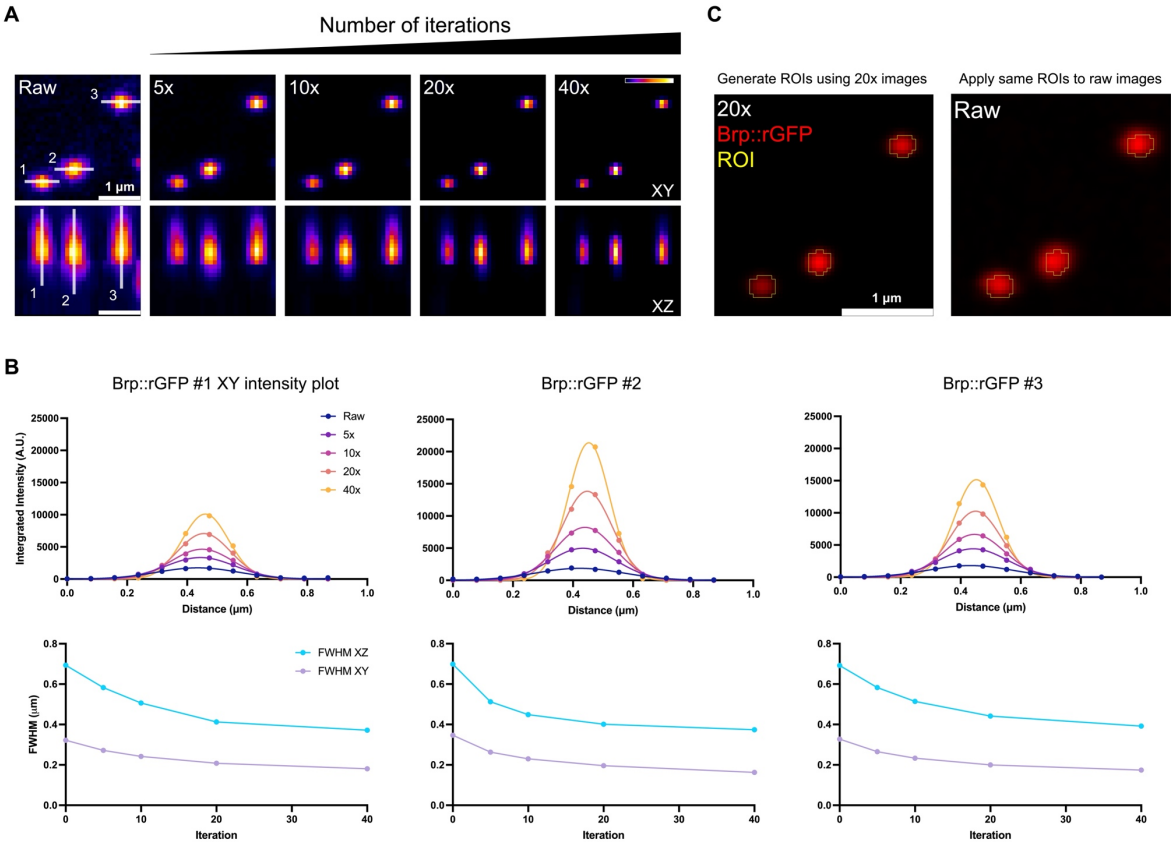

Figure 1 – figure supplement 4 Effect of iterative Richardson-Lucy image deconvolution.

(**A**) Brp::rGFP clusters of a DPM neuron in raw image, and in images deconvolved for 5~40 iterations. Max projections of the XY and XZ planes were shown. White transparent lines indicate pixels where the intensity profiles were plotted in B. Numbers denote different Brp::rGFP clusters. Scale bars, 1 µm.

(**B**) Upper panels show intensity profiles of Brp::rGFP clusters undergone different iterations of deconvolution. Lower panels show the full width at half maximum (FWHM) value of intensity profiles.

(**C**) 3D ROIs were generated using deconvolved images and then were used to analyze the volume and intensity of individual Brp::rGFP clusters in raw images. Scale bars, 1 µm.

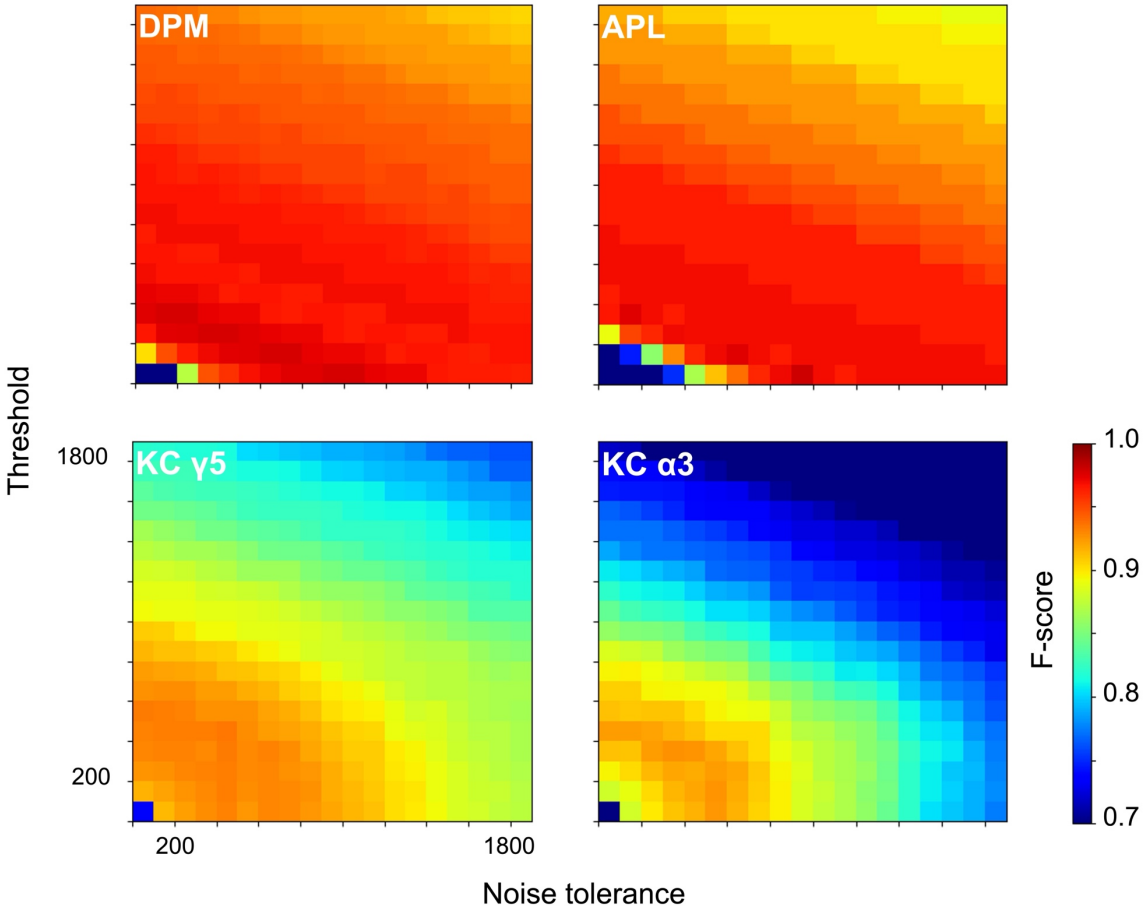

Figure 1 – figure supplement 5 Heatmaps of F-scores showing the performance of the pipeline in detecting individual Brp::rGFP clusters in different cell types.

An intensity threshold (threshold) is applied to reduce background noise when detecting 3D maxima. Noise tolerance adjusts the sensitivity of 3D maxima detection. Color represents F-score value.

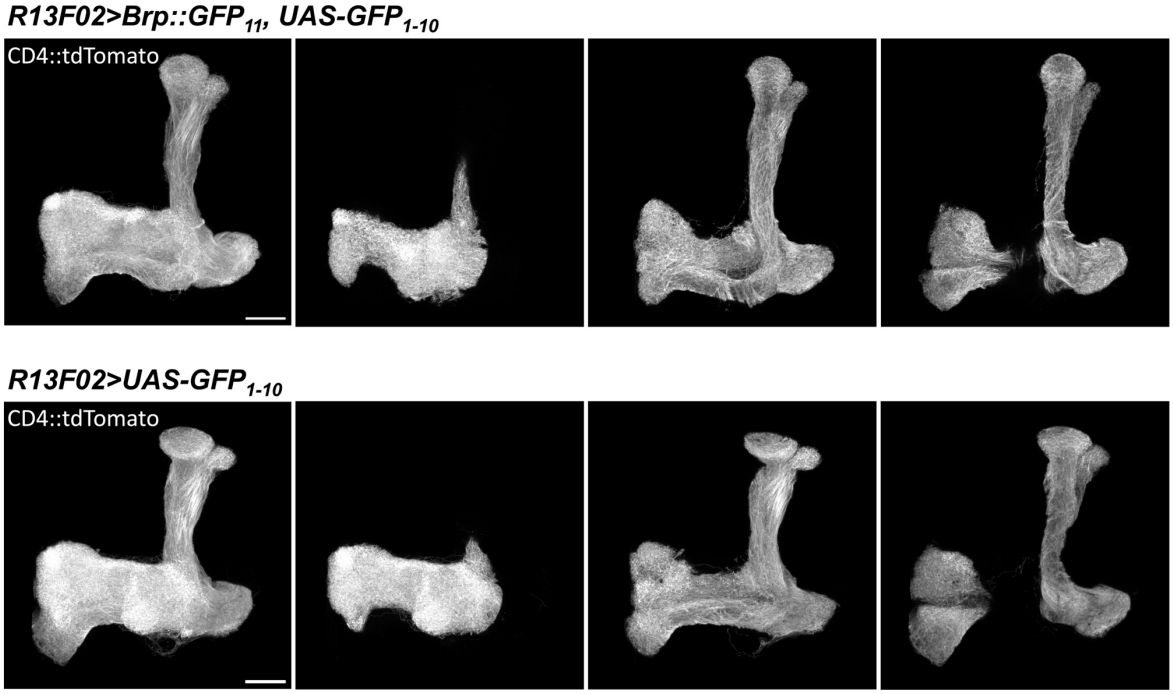

1065

1066 **Figure 7 – figure supplement 1 Gross anatomy of KC terminals is not affected by**

1067 **Brp::rGFP tagging.**

1068 Morphology of KC terminals in flies with or without GFP_{11} insertion. Both groups express

1069 GFP_{1-10} and CD4::tdTomato, driven by *R13F02-GAL4*. Scale bars, 20 μm.

1070

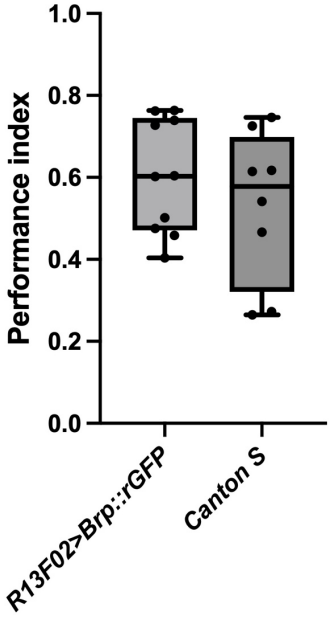

1071

1072 **Figure 7 – figure supplement 2 Brp::rGFP tagging in KCs does not affect short-term**
1073 **memory performance.**
1074 10% 4-MCH or 10% 3-OCT was paired with 90 V electric shocks. Odor preference was
1075 tested immediately after conditioning. GFP reconstitution was induced in KCs using
1076 *R13F02-GAL4*. *R13F02>Brp::rGFP*, n = 10; *Canton S*, n = 8. ns = non-significant.
1077 Welch's t test.
1078

Supplementary files

Supplementary file 1

Python code used for nearest neighbor, local intensity and AZ density analysis.

Supplementary file 2

Example data of a DPM neuron generated by the 3D spot segmentation, before being processed by the analysis code.